



HAL
open science

Microseismic Constraints on the Mechanical State of the North Anatolian Fault Zone 13 Years After the 1999 M7.4 Izmit Earthquake

Eric Beaucé, Robert van der Hilst, Michel Campillo

► **To cite this version:**

Eric Beaucé, Robert van der Hilst, Michel Campillo. Microseismic Constraints on the Mechanical State of the North Anatolian Fault Zone 13 Years After the 1999 M7.4 Izmit Earthquake. *Journal of Geophysical Research: Solid Earth*, 2022, 127 (9), pp.e2022JB024416. 10.1029/2022JB024416 . hal-03798652

HAL Id: hal-03798652

<https://hal.science/hal-03798652>

Submitted on 5 Oct 2022

HAL is a multi-disciplinary open access archive for the deposit and dissemination of scientific research documents, whether they are published or not. The documents may come from teaching and research institutions in France or abroad, or from public or private research centers.

L'archive ouverte pluridisciplinaire **HAL**, est destinée au dépôt et à la diffusion de documents scientifiques de niveau recherche, publiés ou non, émanant des établissements d'enseignement et de recherche français ou étrangers, des laboratoires publics ou privés.

1 **Microseismic Constraints on the Mechanical State of the**
2 **North Anatolian Fault Zone Thirteen Years after the 1999**
3 **M7.4 Izmit Earthquake**

4 **Eric Beauce^{1,3}, Robert D. van der Hilst¹, Michel Campillo^{2,1}**

5 ¹Department of Earth, Atmospheric, and Planetary Sciences, Massachusetts Institute of Technology, USA

6 ²Institut des Sciences de la Terre, Université Grenoble Alpes, France

7 ³Lamont-Doherty Earth Observatory, Columbia University, NY, USA

8 **Key Points:**

- 9 • We build an extensive earthquake catalog using our new fully automated method
10 along the western North Anatolian Fault Zone (NAFZ).
11 • We observe variable statistical properties (b-value, and temporal clustering) along
12 the NAFZ.
13 • High b-value and strong temporal clustering may suggest the occurrence of slow
14 slip in the Lake Sapanca step-over.

Corresponding author: Eric Beauce, ebeauce@ldeo.columbia.edu

Abstract

The 17 August 1999 M_w 7.4 Izmit earthquake ruptured the western section of the North Anatolian Fault Zone (NAFZ) and strongly altered the fault zone properties and stress field. Consequences of the co- and post-seismic stress changes were seen in the spatio-temporal evolution of the seismicity and in the surface slip rates. Thirteen years after the Izmit earthquake, in 2012, the seismic network Dense Array for North Anatolia (DANA) was deployed for 1.5 years. We built a new catalog of microseismicity ($M < 2$) by applying our automated detection and location method to the DANA data set. Our method combines a systematic backprojection of the seismic wavefield and template matching. We analyzed the statistical properties of the catalog by computing the Gutenberg-Richter b-value and by quantifying the amount of temporal clustering in groups of nearby earthquakes. We found that the microseismicity mainly occurs off the main fault and that the most active regions are the Lake Sapanca step-over and near the Akyazi fault. Based on previous studies, we interpreted the b-values and temporal clustering *i*) as indicating that the Akyazi seismicity is occurring in high background stresses and is driven by the Izmit earthquake residual stresses, and *ii*) as suggesting evidence that an intricate combination of seismic and aseismic slip was taking place on heterogeneous faults at the eastern Lake Sapanca, near the brittle-ductile transition. Combined with geodetic evidence for enhanced north-south extension around Lake Sapanca following the Izmit earthquake, the seismicity supports the possibility of slow slip at depth in the step-over.

Plain Language Summary

On 17 August 1999, a large M7.4 earthquake struck near the city of Izmit, in western Turkey, and caused important human and material losses. The earthquake resulted from the large and sudden displacement of crustal blocks along the North Anatolian Fault Zone (NAFZ). Transient changes in the crustal and fault properties are commonly observed following such large events. In this study, we analyze the statistical properties of microearthquakes, that is, of small earthquakes ($M < 2$) typically too small to affect the surrounding population, to gain knowledge about the state of the NAFZ more than a decade after the Izmit earthquake. First, we address the challenge of locating microearthquakes, in space and time, by applying our automatic earthquake detection and location algorithm. Then, we use a statistical analysis to characterize physical properties of the NAFZ and, thus, to highlight the peculiar properties of faults near Lake Sapanca. We interpret that these faults are heterogeneous and slip both seismically and aseismically. Our study calls for taking a closer look at the extension across Lake Sapanca with different, complementary geophysical methods.

1 Introduction

The North Anatolian Fault Zone (NAFZ) is a 1,500 km long strike-slip fault that bounds the Anatolian plate to the south and the Eurasian plate to the north (Figure 1A). The fault slips, overall, in a right-lateral manner to accommodate the westward motion of Anatolia with respect to Eurasia due to the combination of the subduction along the Hellenic trench and the Cyprus trench in the southwest and the south and the collision with Arabia in the southeast (Le Pichon & Angelier, 1979; McClusky et al., 2000; Reilinger et al., 2006). Near the Gulf of Izmit, in western Turkey, the NAFZ splits into a northern strand and a southern strand. These two strands bound the Almacik mountains in the east and the Armutlu block in the west, and separate the Istanbul Zone in the north from the Sakarya Terrane in the south, which are the remains of the passive margin of the Intra-Pontide Ocean (see Figure 1B, e.g. Akbayram et al., 2013). Most of the deformation is accommodated on the northern strand (e.g. Meade et al., 2002; Reilinger et al., 2006).

The 17 August 1999 M7.4 Izmit earthquake and the 12 November 1999 Düzce M7.2 earthquake are the most recent (as of the time of writing) events of a series of westward

65 migrating $M > 7$ earthquakes that ruptured almost entirely the North Anatolian Fault Zone
66 (e.g. Toksöz et al., 1979; Stein et al., 1997). The Izmit earthquake nucleated near the Izmit
67 Bay, propagated bilaterally and broke a 150 km-long, almost vertical section of the fault
68 made of four, or five, segments along the northern strand (Toksoz et al., 1999; Barka et
69 al., 2002). To the east, the rupture propagated at super-shear speeds (Bouchon et al., 2001,
70 2011) and broke the Izmit-Sapanca, the Sapanca-Akyazi and the Karadere segments (cf.
71 names on Figure 1B). To the west, the rupture propagated along the Gölcük segment and
72 stopped on the Yalova segment (Langridge et al., 2002), increasing the probability of ma-
73 jor failure further west beneath the Marmara Sea (Parsons et al., 2000). The Düzce earth-
74 quake nucleated near the eastern termination of the Izmit earthquake, likely due to in-
75 creased Coulomb stress (Parsons et al., 2000; Utkucu et al., 2003). The co- and post-seismic
76 stress changes and the transient changes of the fault's mechanical properties caused by
77 the Izmit earthquake affected the local seismicity patterns and the focal mechanisms of
78 microearthquakes (e.g. Bohnhoff et al., 2006; Pınar et al., 2010; Ickrath et al., 2015). GPS
79 and interferometric synthetic aperture radar (InSAR) observations suggest that fast and
80 rapidly decaying afterslip occurred in the middle-to-lower crust in the months following
81 the Izmit-Düzce earthquake sequence (e.g. Reilinger et al., 2000; Bürgmann et al., 2002),
82 then relayed by slower post-seismic slip at depth (Ergintav et al., 2009; Hearn et al., 2009).
83 Patterns of surface displacement also suggest the existence of shallow creep along the
84 Izmit-Sapanca and the Sapanca-Akyazi segments (e.g. Çakir et al., 2012; Hussain et al.,
85 2016). Transient creep episodes have been identified more than a decade after the Izmit
86 earthquake (Aslan et al., 2019).

87 Despite the overall good understanding of the east-west motion along the west-
88 ern NAFZ, smaller scale, north-south extension at some locations remains enigmatic. Co-
89 and post-seismic slip on vertical fault segments seems unable to reproduce the patterns
90 of north-south extension observed in geodetic data (e.g. Ergintav et al., 2009; Hearn et
91 al., 2009). Even though refining the geometry of the main fault segments of the NAFZ
92 helps explain the observations (e.g. slightly north dipping faults, Cakir et al., 2003), mod-
93 els of the post- and inter-seismic deformation along the NAFZ would benefit from tak-
94 ing into account secondary structures, such as the faults in step-overs. Microseismicity
95 ($M < 2$) provides information at small length scales at seismogenic depths and thus is com-
96 plimentary to geodetic data in building a better understanding of slip along the NAFZ (aseis-
97 mic vs seismic, distributed vs localized), that is, of its mechanical state.

98 The abundance of microearthquakes makes them well-suited for statistical analy-
99 ses. Of interest here are the b -value of the Gutenberg-Richter law (Gutenberg & Richter,
100 1941) that describes the frequency-magnitude distribution of a population of earthquakes,
101 and the fractal dimension D of the earthquake occurrence time series (Smalley Jr et al.,
102 1987; Beaucé et al., 2019) that quantifies the strength of temporal clustering. The b -value
103 acts as a stressmeter (Amelung & King, 1997; C. H. Scholz, 2015), and the fractal dimen-
104 sion D is related to the density of fractures and seismic-aseismic slip partitioning (C. Scholz,
105 1968; Dublanchet et al., 2013).

106 The dense seismic array DANA (Dense Array for North Anatolia DANA, 2012, see
107 Figure 1C) was deployed around the rupture trace of the 1999-08-17 $M 7.4$ Izmit earth-
108 quake, it operated from early May 2012 to late September 2013. These data enabled mul-
109 tiple studies that improved our understanding of the complex structures and seismicity
110 patterns in the region (e.g. Poyraz et al., 2015; Kahraman et al., 2015; Papaleo et al., 2018;
111 Taylor et al., 2019). Here, we study microearthquakes in order to improve our understand-
112 ing of the mechanical state of the North Anatolian Fault Zone more than a decade after
113 the Izmit earthquake. First, we briefly describe our automated earthquake detection and
114 location method (Section 3), and then present the earthquake catalog (Section 4.1) and
115 a statistical analysis of collective properties of earthquakes (b -value, Section 4.2, and tem-
116 poral clustering, Section 4.3). These observations allow a characterization of the phys-
117 ical environment in which seismicity takes place. We interpret and discuss our results to
118 question the role of secondary structures in the dynamics of NAFZ (Section 5).

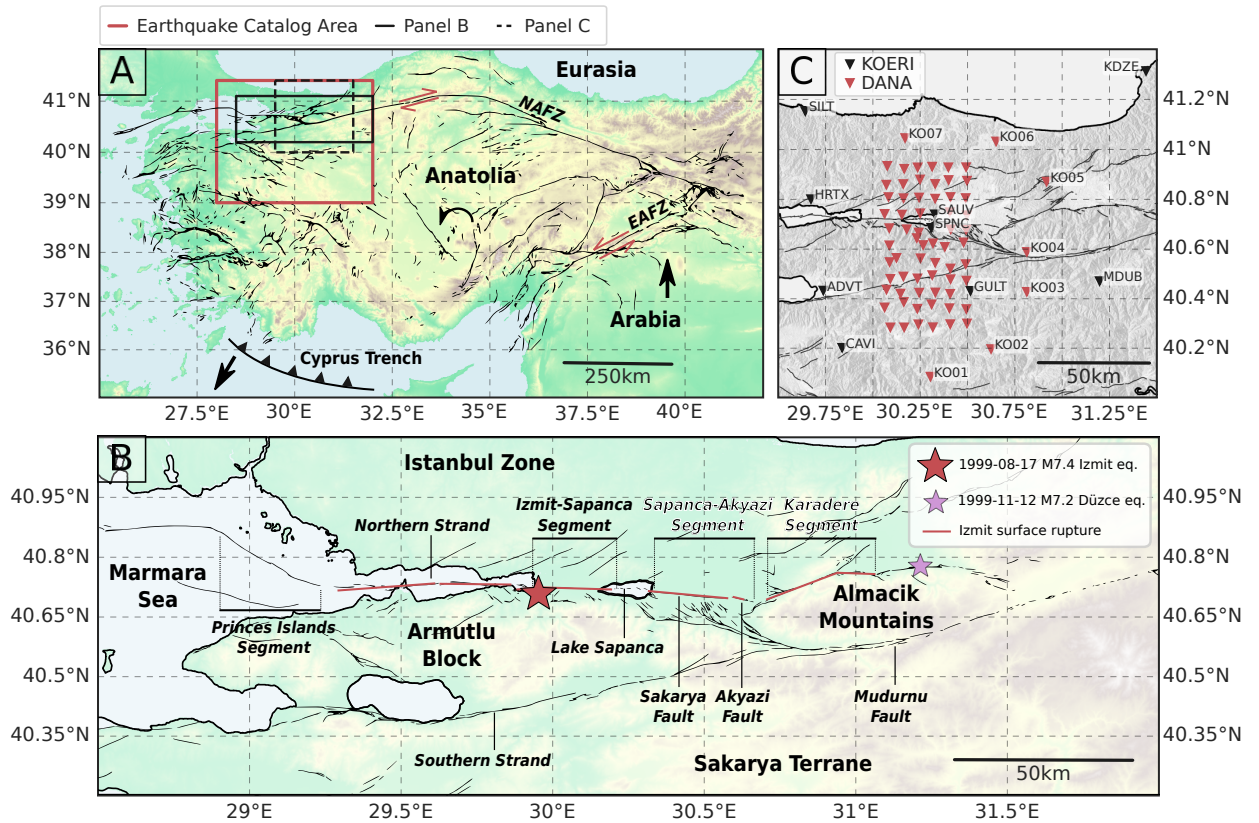


Figure 1. **A:** Large scale view of the North Anatolian Fault Zone. Abbreviations: NAFZ - North Anatolian Fault Zone, EAFZ - East Anatolian Fault Zone. The red arrows indicate the direction of coseismic motion. Our study region is located at the western end of the NAFZ. **B:** Magnified view of the fault zone in our study region. Larger font names are the main geologic units: Istanbul Zone, Armutlu Block, Almacik Mountains and Sakarya Terrane. The smaller font, italic names are segments and faults of the NAFZ: the Izmit-Sapanca segment, the Sapanca lake step-over, the Sapanca-Akyazi segment (which together constitute the northern strand), the Karadere segment and the southern strand (names following Barka et al., 2002). The Sapanca-Akyazi segment is made of the Sakarya fault and the Akyazi fault. The flat area around the Akyazi fault is referred to as the Akyazi plain. Both Lake Sapanca and the Akyazi plain are pull-apart basins. The large red star indicates the epicenter of the M_w 7.4 Izmit earthquake, and the small purple star indicates the epicenter of the M_w 7.2 Düzce earthquake. **C:** The seismic stations used in this study are from the temporary experiment DANA (70 stations, red triangles; DANA, 2012) and the permanent network KOERI (9 stations, black triangles; Kandilli Observatory And Earthquake Research Institute, Boğaziçi University, 1971). Each column of the DANA array is indexed by a letter and each row is indexed by a number (DA01, DA02, ..., DB01, ...).

119

2 Data

120

121

122

123

124

125

The continuous seismic data were recorded by broadband stations from the temporary array DANA (70 stations) and the permanent network KOERI (9 stations, see the locations in Figure 1, and the Data and Resources section). The time period covered by this study is set by the duration of the DANA experiment: 2012-05-04 to 2013-09-20. Sampling rates are 50 Hz for all stations but SAUV, which samples at 100 Hz. We band-pass filtered the data between 2 Hz and 12 Hz to eliminate low frequency noise and to

126 allow us to downsample the time series to 25 Hz in order to make the computation less
127 intensive.

128 3 Methodology

129 3.1 Earthquake Detection, Location, and Magnitude Estimation

130 We analyzed the data for the entire time period with a fully automatized earthquake
131 detection and location method. The core of the workflow, summarized in Figure 2, con-
132 sists of three stages:

- 133 1. Backprojection (Section 3.1.1): The energy of the seismic wavefield is continuously
134 backprojected onto a 3D grid of potential sources to detect coherent (earthquake)
135 sources.
- 136 2. Relocation (Section 3.1.2): The P- and S-wave first arrivals of the previously de-
137 tected events are identified with the automatic phase picker PhaseNet (Zhu & Beroza,
138 2019), and the picks are used in the NonLinLoc earthquake location software (Lomax
139 et al., 2000, 2009).
- 140 3. Template matching (Section 3.1.3): The successfully relocated earthquakes are used
141 as template earthquakes in a matched-filter search to detect other, smaller earth-
142 quakes in the same region using the Fast Matched Filter software (Beaucé et al.,
143 2018).

144 The detection method is discussed in detail in Beaucé et al. (2019), but the relocation is
145 now fully automated and includes PhaseNet and NonLinLoc. In an extra step, we further
146 characterized the detected earthquakes by relocating them with the double-difference
147 method (Section 3.1.4) and estimating their magnitude (Section 3.1.5).

148 3.1.1 Backprojection and Location

149 We backprojected the energy of the seismic wavefield recorded at the array of seis-
150 mic stations onto a 3D grid of potential sources beneath the study region, searching for
151 the space-time locations of coherent sources. We computed the composite network re-
152 sponse (CNR, Frank & Shapiro, 2014):

$$153 \text{CNR}(t) = \max_k \{ \text{NR}_k(t) \}; \quad \text{NR}_k(t) = \sum_{s,c} \text{env} \left(u_{s,c}(t + \tau_{s,c}^{(k)}) \right). \quad (1)$$

154 In this equation, t is the detection time and $\text{NR}_k(t)$ is the network response for source
155 location indexed by k at time t . $\text{NR}_k(t)$ is the sum of the envelopes (the modulus of the
156 analytical signal) of the seismograms $u_{s,c}$ shifted in time by the moveout $\tau_{s,c}^{(k)}$ on station
157 s and component c . The moveouts were computed using the ray-tracing software Pykonal
158 (White et al., 2020) in the 1D velocity model from Karabulut et al. (2011) (see Table S1).
159 We note that the use of a 1D velocity model in this region can introduce significant er-
160 rors in the earthquake locations because of the strong lateral velocity variations, in par-
161 ticular across the two strands of the NAFZ (e.g. Karahan et al., 2001; Kahraman et al., 2015;
162 Papaleo et al., 2018). This velocity model produced a visually satisfying agreement be-
163 tween earthquake epicenters and fault surface traces, and allowed consistency with a pre-
164 vious study on the same data set (Poyraz et al., 2015). The backprojection method nat-
165 urally provides an estimate of the location of each detected events. However, the net-
166 work response finds the times that aligned the envelope maxima rather than the P- and
167 S-wave arrivals, which results in approximate locations.

168 3.1.2 Relocation

169 All the events detected through the CNR were processed with the deep neural net-
170 work PhaseNet (Zhu & Beroza, 2019) to automatically pick the P- and S-wave first arrivals.

Earthquake Detection and Location Workflow

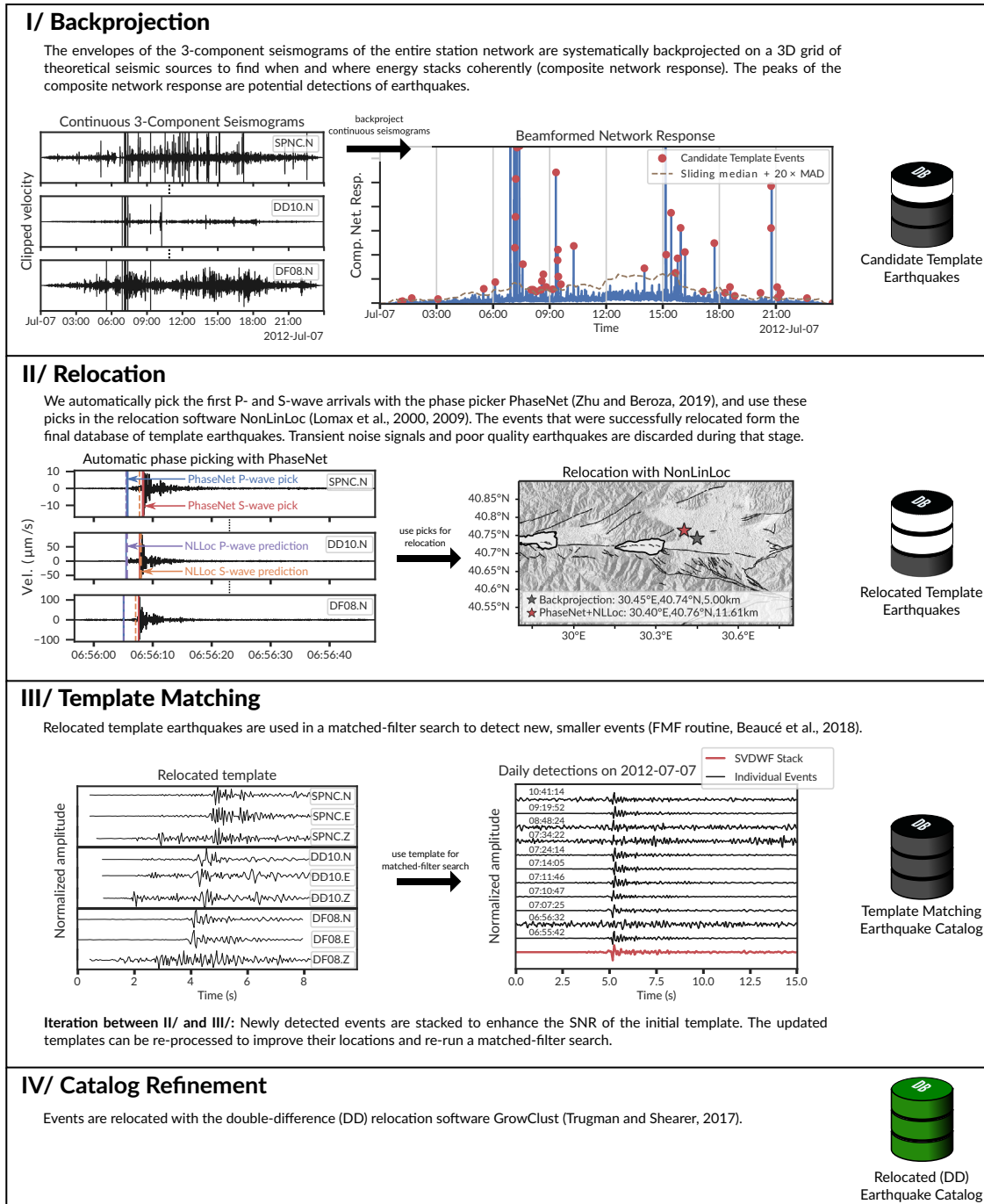


Figure 2. Summary flowchart of the earthquake detection and location method. For clarity, only a subset of stations are shown in the above panels, but all the analysis is carried on the 79 stations together. Template matching is performed on the 10 stations closest to the source and the detection threshold is set to $8 \times \text{RMS}$ of the correlation coefficients in a 30-minute sliding window. See Data and Resources for code availability.

171 These picks were then used by the location software NonLinLoc (Lomax et al., 2000, 2009)
 172 to get the earthquake locations and their uncertainties given as $1-\sigma$ intervals. We required

173 at least four P- and S-wave picks and a total minimum of 15 picks to relocate an event.
 174 Requiring both P- and S-wave picks helps constrain the earthquake depth, and impos-
 175 ing at least 15 picks efficiently reduced the number of solutions with very large uncer-
 176 tainties. Events that could not be successfully relocated with NonLinLoc (e.g. noisy picks,
 177 multiple sources recorded at the same time) were discarded. More information about the
 178 input parameters used by PhaseNet and NonLinLoc can be found in Text S1 of Support-
 179 ing Information S1.

180 **3.1.3 Template Matching**

181 Successfully relocated events were kept as templates and used in a matched-filter
 182 search to detect new, smaller magnitude earthquakes. Template matching is a powerful
 183 method for detecting low signal-to-noise ratio (SNR) events given prior knowledge of the
 184 target seismicity (e.g. Gibbons & Ringdal, 2006; Shelly et al., 2007; Ross et al., 2019). It
 185 consists of searching for all earthquakes with similar waveforms and moveouts to a known
 186 earthquake, that is, earthquakes sharing a similar location and focal mechanism. The sim-
 187 ilarity is measured by the network-averaged correlation coefficient (CC) between the tem-
 188 plate waveforms $T_{s,c}$ and the seismograms $u_{s,c}$ shifted by the template moveout $\tau_{s,c}$:

$$189 \quad \text{CC}(t) = \sum_{s,c} w_{s,c} \sum_{n=1}^N \frac{T_{s,c}(t_n) u_{s,c}(t + t_n + \tau_{s,c})}{\sqrt{\sum_{n=1}^N T_{s,c}^2(t_n) \sum_{n=1}^N u_{s,c}^2(t + t_n + \tau_{s,c})}}, \quad (2)$$

190 where $w_{s,c}$ is the weight attributed to station s , component c , and N is the length of the
 191 template waveforms. We ran the matched-filter search on multiple nodes of a super-computer
 192 equipped with Graphic Processing Units (GPUs) using the template matching software
 193 Fast Matched Filter (Beaucé et al., 2018). We used a template window of 8 seconds start-
 194 ing 4 seconds before the S wave on the horizontal components and 1 second before the
 195 P wave on the vertical components. We used a detection threshold of 8 times the root
 196 mean square (RMS) of the CC time series in a 30-minute sliding window ($8 \times \text{RMS}\{\text{CC}(t)\}$).
 197 The 8 s template duration is adequate given the signal duration of small magnitude earth-
 198 quakes at ~ 10 -50 km source-receiver distances. The $8 \times \text{RMS}$ threshold is in the con-
 199 servative range of commonly used threshold in template matching studies (e.g. Shelly et
 200 al., 2007; Ross et al., 2019). Note that $8 \times \text{RMS}$ is about 12 times the median absolute
 201 deviation (MAD) for a gaussian distribution.

202 After a matched-filter search over the whole study period, each template earthquake
 203 has detected potentially many new similar earthquakes. We leveraged the similarity of
 204 the detected events to form higher SNR waveforms with the Singular Value Decompo-
 205 sition and Wiener Filtering method (Moreau et al., 2017), for the efficient extraction of
 206 coherent signal and waveform denoising. The new, higher SNR template earthquakes were
 207 in turn used to refine the locations and run another iteration of the matched-filter search.
 208 We iterated the detection-stacking-relocation workflow only once to trade-off SNR im-
 209 provement and loss of high frequency information due to stacking.

210 Neighboring templates often detect the same events, therefore we kept a single event
 211 out of all detections occurring within three seconds of each other, from templates whose
 212 uncertainty ellipsoids were separated by less than 5 km, and with average waveform sim-
 213 ilarity greater than 0.33. These thresholds were chosen based on physical considerations
 214 (the time threshold 3 sec assumes location errors of up to 10-15 km, the space thresh-
 215 old 5 km accounts for coherency of waves at 2 Hz, etc) and empirically by inspecting the
 216 output catalog for duplicated events.

217 **3.1.4 Double-Difference Relative Relocation**

218 We refined the earthquake locations in the region of interest, near the NAFZ and
 219 beneath the stations, with the double-difference relative relocation method (e.g. Poupinet
 220 et al., 1984; Waldhauser & Ellsworth, 2000). P- and S-wave differential arrival times were
 221 computed by finding the lag times that maximize the inter-event correlation coefficients

and summing them to the travel time differences. The differential times were then processed by the relocation software GrowClust (Trugman & Shearer, 2017, additional information on parameters are given in supplementary information, Text S1.4). GrowClust estimates location uncertainties with the non-parametric bootstrap resampling method (Efron & Tibshirani, 1986).

3.1.5 Magnitude Estimation

Local magnitudes were computed from the amplitude ratios of peak velocities. This required estimating the magnitude of at least one event per template to calibrate our local magnitude scale. Therefore, we computed the moment magnitude M_w by fitting the Brune model (Equation (3), Brune, 1970) to the multi-station average displacement spectra that satisfied an SNR criterion (see details in supplementary Text S1.6 and Figure S1).

$$|u_{\text{Brune}}(f)| = \frac{\Omega_0}{\left(1 + \frac{f}{f_c}\right)^2}. \quad (3)$$

In Equation (3), Ω_0 is the low-frequency plateau, which is proportional to the seismic moment M_0 , and f_c is the corner frequency. Additional information on how we corrected the spectra for geometrical spreading and attenuation to compute M_0 from Ω_0 is given in Text S1.6. The moment magnitude M_w is:

$$M_w = \frac{2}{3} (\log M_0 - 9.1). \quad (4)$$

Once moment magnitude estimates were available for at least one event in a template family, we estimated a local magnitude M_L for all other events based on log amplitude ratios (details in Text S1.6). Finally, we measured the scaling between M_w and M_L and built the calibration first-order relationship $M_w = A + BM_L$ (see Figure S1B).

3.1.6 Identifying Mining-Related Seismicity

Template matching lends itself particularly well to identifying sources of mining-related earthquakes. We identified these by analyzing the distribution of detection times within the day. Templates that detected more than 80% of events between 6am and 6pm were categorized as mining-related templates (see Figure S3), since we do not expect natural seismicity to occur within preferred times.

3.2 Gutenberg-Richter b-value

The frequency-magnitude distribution of earthquakes typically follows the Gutenberg-Richter law (Gutenberg & Richter, 1941):

$$\log N(M) = a - bM. \quad (5)$$

In Equation (5), $N(M)$ is the number of earthquakes exceeding magnitude M , the a-value depends on the total number of observed events, and the b-value controls how frequent larger earthquakes are (typically $b \approx 1$). We estimated the b-value with the maximum likelihood technique (Aki, 1965):

$$b = \frac{1}{\ln(10) (\bar{M} - M_c)}. \quad (6)$$

Equation (6) is derived for continuous magnitudes M (no bias from binned magnitudes). M_c is the magnitude of completeness, *i.e.* the magnitude above which all events are detected. We computed M_c with the maximum curvature technique (*e.g.* Wiemer & Katsumata, 1999, , see Figure S2). Additional information on the computation of M_c and b is given in the supporting information (see Text S1.7 and Figure S2).

At each template location, we selected all the templates within a 5 km-radius and used the events they detected to compute b and M_c . Following Tormann et al. (2013), we imposed a minimum of 50 events to compute the b -value and, in addition, requested a minimum of 30 events above the magnitude of completeness. As these numbers are still low, we carefully estimated the uncertainties to assess the statistical significance of b -value differences between different groups following Utsu (1966). The statistical test is described in detail in Text S1.7 and illustrated in Figure S2.

3.3 Temporal Clustering

We refer to temporal clustering as the tendency of earthquakes to influence the timings (advance or delay) of future earthquakes, that is, the non-randomness of earthquake sequences (e.g. Gardner & Knopoff, 1974; Marsan & Lengline, 2008). We quantified the strength of temporal clustering in earthquake sequences by analyzing the statistical properties of the number of earthquakes per unit time, which we refer to as the earthquake occurrence time series:

$$e(t) = \text{Number of events} \in [t; t + \Delta t], \quad (7)$$

where Δt is a user-defined time bin duration, and t is the calendar time. An example is given in Figure 3A. Burst-like sequences covering wide intervals of recurrence times are not random (see Figure 3B,C) but clustered in time. Time clustered seismicity exhibits time scale invariant characteristics. The spectrum of the earthquake occurrence $e(t)$ follows a power law of frequency ($\propto f^{-\beta}$, see Figure 3D), and the time series $e(t)$ shows a fractal statistics (Figure 3E). We measured the fractal dimension of $e(t)$ by subsequently dividing the time axis into smaller and smaller time bins (varying size τ), and counting the fraction of bins x that were occupied by at least one earthquake (Smalley Jr et al., 1987; Lowen & Teich, 2005). For a certain range of time bin sizes τ , we observe:

$$x \propto \tau^{1-D}. \quad (8)$$

In Equation (8), D is the fractal dimension of the time series. The fractal dimension varies between the two end-members $D = 0$ for a point process (e.g. Poisson point process for the background seismicity), and $D = 1$ for a line (uninterrupted seismicity). A large fractal dimension ($D > 0.2$) characterizes cascade-like activity where past events strongly influence the timings of future events. Fractal analysis has been used in multiple studies to characterize earthquake clustering (Smalley Jr et al., 1987; Lee & Schwarcz, 1995; Beaucé et al., 2019). Note that periodic seismicity does not follow a fractal behavior and cannot be characterized by this method. Building the $x(\tau)$ curve (Equation (8), Figure 3E) is computationally more simple than estimating the spectrum (Figure 3D). Likewise, it is simpler to fit $x(\tau)$. Therefore, we chose to compute the fractal dimension D to characterize temporal clustering in the rest of this study.

The method described in Section 3.3 does not explicitly deal with space. However, we applied this analysis to subsets of the earthquake catalog containing neighboring earthquakes (as described for the b -value, see Section 3.2), and thus obtained a fractal dimension for each template.

4 Results

4.1 The Earthquake Catalog

Our earthquake catalog and detection and location codes are available online (see Data and Resources, and see the supplementary information for details on the structure of the catalog file).

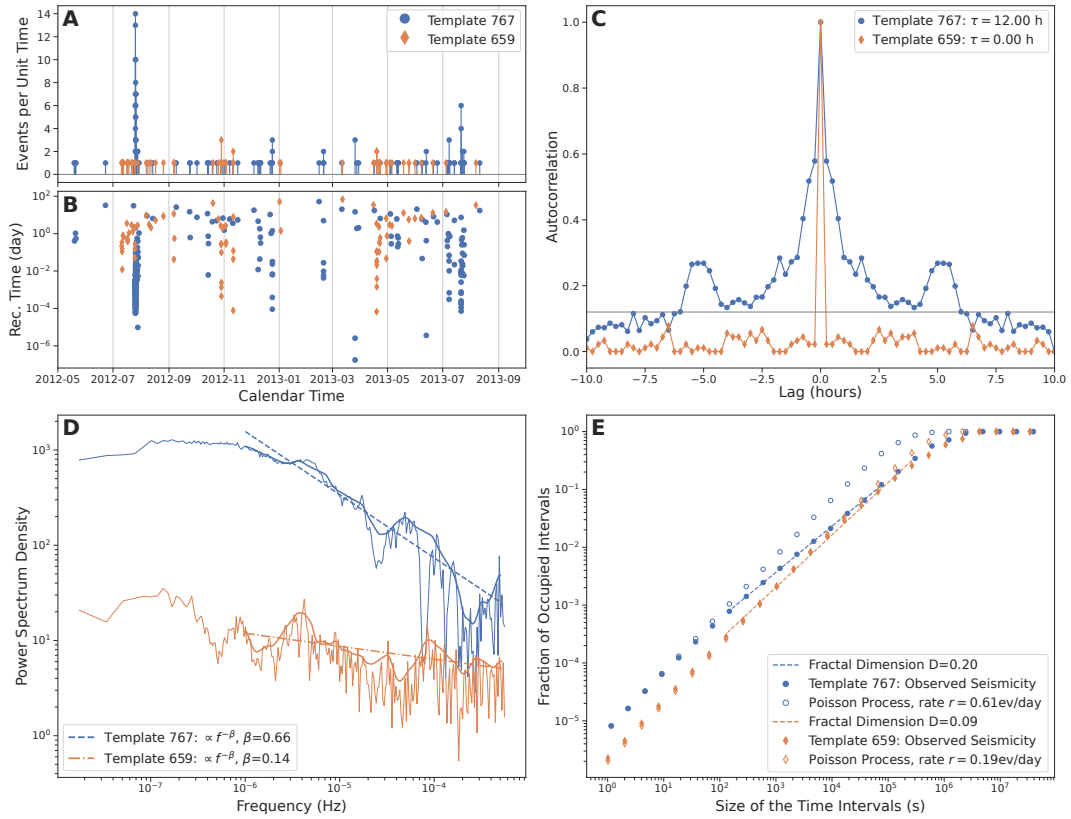


Figure 3. Quantifying the strength of temporal clustering in a strongly clustered sequence (Template 767, blue dots) and a weakly clustered sequence (Template 659, orange diamonds). **A:** Number of earthquakes per unit time (referred to as earthquake occurrence, see Equation (7)). **B:** Recurrence times vs. origin times. **C:** Autocorrelation of the earthquake occurrence time series. The horizontal black line is the arbitrary threshold used to define the correlation time τ . **D:** Power spectral density of the earthquake occurrence. The linear trend, in the log-log space, is the exponent of the power-law that indicates a scale invariant process. **E:** Fractal analysis of the earthquake occurrence (see text and Equation (8)). We measure the slope between $dt_{\min}=100$ s and $dt_{\max} = 1/r$, where $r = N/T$ is the average seismic rate (number of events N divided by time span T). For reference, for each template we simulate the seismicity from a Poisson point process with average rate r . The slope of the Poisson point process gives a fractal dimension $D = 0$ (i.e. dimension of a point).

308

4.1.1 Regional Seismicity

309

310

311

312

313

314

315

316

317

318

319

320

Following the method described in Section 3.1, we built a database of 3,546 templates and with them detected 35,437 events, including both natural and anthropogenic seismicity. We applied our analysis between 38.50°N-41.50°N and 28.00°E-32.00°E (see Figure 1A). Figure 4 shows the locations of the 3,320 template earthquakes that are shallower than 20 km and have horizontal uncertainties less than 15 km, as well as the cumulative detection count per template over the whole study period. We purposely present an earthquake catalog for this region that extends far beyond the NAFZ to provide a comprehensive description of the earthquake signals found in the data set. We found that most of the 1,972 events detected with templates located deeper than 20 km originated far outside the study region, in particular in the Hellenic and Cyprus subduction zones in the southwest and south of the study region, respectively. Therefore, we discarded these deeper templates for any further analysis. Furthermore, we found that about half

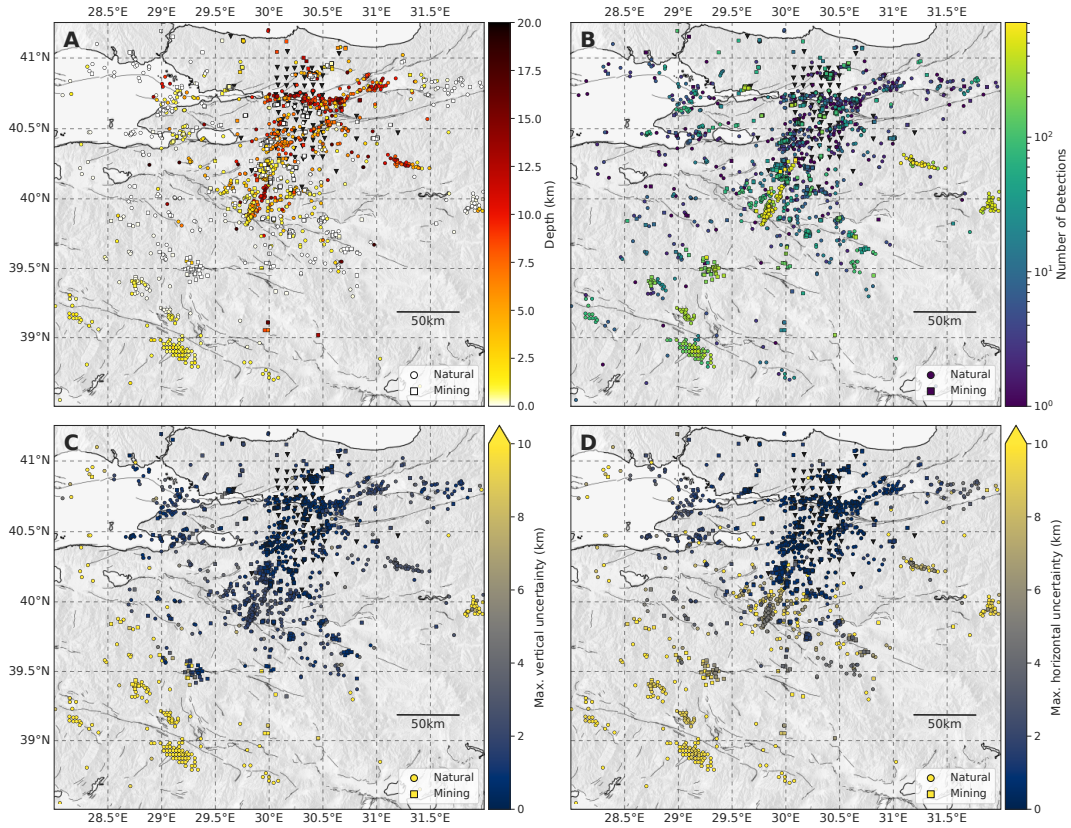


Figure 4. Map view of the locations of the template earthquakes detected and used in this study. Only templates with maximum horizontal uncertainty less than 15 km and depth less than 20 km are shown (total of 3,320 templates). Filled dots are for natural earthquakes (1,471 templates), and squares are for mining-related events (1,849 templates; see text for details about identifying templates as mining templates). **A:** Event depths. **B:** Cumulative number of event detections per template. Most of the detected earthquakes actually originate from outside the North Anatolian Fault Zone. **C:** Maximum vertical uncertainty v_{\max} , i.e. depth range spanned by the projection of the uncertainty ellipse onto a vertical plane. **D:** Maximum horizontal uncertainty h_{\max} , i.e. length of the major semi-axis of the projection of the uncertainty ellipse onto the horizontal plane.

321 of the detected seismicity was due to mining activity (see Section 3.1.6): among the 31,329
 322 earthquakes detected with the 3,320 templates, we identified 16,674 natural earthquakes
 323 and 14,655 mining-related earthquakes. The locations of mining activity that we iden-
 324 tified (see Figure 4) agree well with the analysis of Poyraz et al. (2015) (their Figure 3) whereas
 325 the Kandilli catalog (see Data and Resources) tends to report less explosions, in partic-
 326 ular beneath the DANA array (see Figure S4).

327 The majority of earthquakes occurred outside the station array and not in the NAFZ
 328 itself, that is, north of 40.80°N or south of 40.30°N (see Figure 4B). Location uncertain-
 329 ties increase with increasing distance from the DANA array: inside 40.30°N-41.00°N and
 330 30.00°E-30.50°E, the average horizontal uncertainty is $\bar{h}_{\max} = 0.97$ km and the average
 331 vertical uncertainty is $\bar{v}_{\max} = 0.74$ km, whereas these uncertainties increase to $\bar{h}_{\max} =$
 332 8.53 km and $\bar{v}_{\max} = 4.57$ km outside this box (see Figure 4C,D).

333 Since accurate moment magnitude estimation rely on correct source-receiver dis-
 334 tances (see Section 3.1.5), we only computed moment magnitudes for events with $h_{\max} <$
 335 5 km (see Figure 4D). After the SNR criterion, we could estimate moment magnitudes within

336 168 template families of natural seismicity, from which we computed 1,929 local mag-
 337 nitudes. These magnitudes range from -1 to 4, and we obtained $b = 0.85$ and $M_c = 1.18$
 338 (see Section 3.2 and Figure S5). We computed a $M_w - M_L$ calibration close to identity, $M_w =$
 339 $0.15 + 0.93M_L$ (see Section 3.1.5 and Figure S1B). The magnitude of completeness of
 340 our catalog indicates that we were not able to estimate magnitudes below $M \approx 1$ but
 341 still detected them: only 12% of the detected seismicity has a magnitude estimate. There-
 342 fore, $M_c = 1.18$ is only an upper bound to the magnitude of completeness of the whole
 343 catalog. For reference, we estimated a b-value and magnitude of completeness of $b =$
 344 0.91 and $M_c = 1.05$ with the catalog published in Poyraz et al. (2015), with magnitudes
 345 ranging from 0 to 4 (see Figure S5). Our magnitudes seemed to be systematically larger
 346 than theirs for smaller events, with an average difference of 0.5 unit over all compared
 347 events (see Figure S5C). Detailed b-values and magnitudes of completeness are presented
 348 in Section 4.2.

349 We present the spatio-temporal distribution of the seismicity in Figure 5. An over-
 350 all decaying activity of natural earthquakes is superimposed to a uniform mining-related
 351 activity (compare Figure 5A vs. B). We observe two sequences of slowly decaying activ-
 352 ity below 39°N and around 40°N . The southernmost earthquake sequence (39°N) is part
 353 of the aftershock activity of the M5.1 2012-05-03 $39.18^\circ\text{N}/29.10^\circ\text{E}/5.4$ km earthquake
 354 (just before the deployment of DANA). The 40°N sequence is not featured in the Kandilli
 355 nor in the United States Geological Survey catalog.

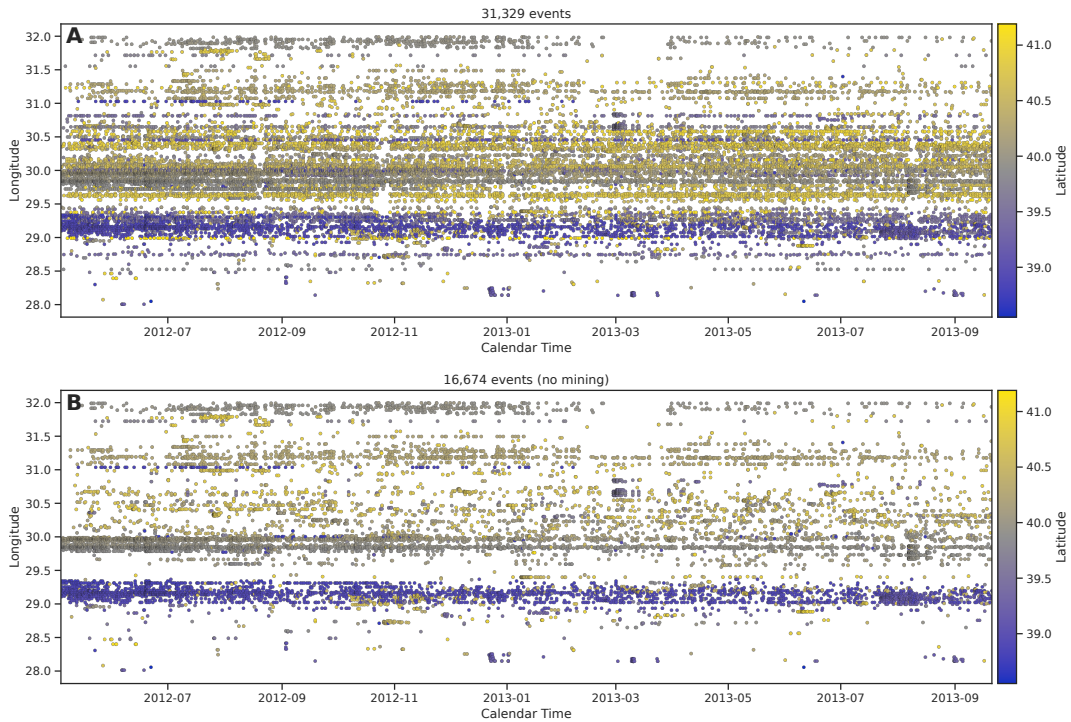


Figure 5. Spatio-temporal distribution of the earthquake activity in the study region. The longitude of each event is shown against its origin time, and the color codes the latitude. **A:** We detected 31,329 events with the 3,320 template earthquakes presented in Figure 4 from 2012-05-04 to 2013-09-20. **B:** The templates due to natural seismicity detected 16,674 earthquakes. The seismic activity taking place on the NAFZ (latitudes 40.35°N - 40.80°N) represents a small amount of the total seismicity ($\sim 2,000$ events).

356

4.1.2 Seismicity of the North Anatolian Fault Zone

357

358

359

360

361

362

363

364

365

366

367

368

369

370

371

372

373

374

375

376

377

378

379

380

381

382

383

384

385

386

387

388

389

390

391

392

393

394

395

396

397

398

399

400

401

402

403

404

405

406

407

408

409

410

Here, we focus on the template earthquakes located in the vicinity of the NAFZ and near the station array (40.25°N-41.00°, 29.80°E-31.00°E). Figure 6 shows the locations of these template earthquakes, as well as the 2,141 earthquakes relocated with the double-difference method (see Section 3.1). The median horizontal and vertical errors on relative locations are 73 m and 91 m, respectively, meaning that they can reliably be interpreted in terms of active structures. Earthquake hypocenters reveal a complex network of faults, with much of the seismicity occurring on secondary faults rather than on the NAFZ itself. We divided the fault zone into nine subregions (*cf.* Figure 6A) whose names we will keep referring to in this manuscript. These are organized into four along-strike sections: Izmit-Sapanca, fault-parallel Sapanca-Akyazi, Karadere, and the entire southern strand, and six fault-perpendicular sections: Lake Sapanca west and east, fault perpendicular Sapanca-Akyazi, Akyazi, and the southern strand west and east. The northern strand is overall more active than the southern strand, and the Sapanca-Akyazi segment hosts the densest activity. In particular, both terminations of the segment, the eastern side of Lake Sapanca and the area around the Akyazi fault, host strong seismicity. The Akyazi region features the deepest seismicity in the vicinity of the NAFZ (down to 20 km). The group of earthquakes located at the northernmost of the Sapanca-Akyazi region (Figure 6A-B) are part of the 2012-07-07 M_L 4.1 Serdivan earthquake sequence. Most of the seismicity along the southern strand occurs in areas where surface fault traces indicate more structural complexity. Note that the relocated seismicity tends to be distributed in patches, which is partly due to the detection method. Indeed, template matching tends to detect groups of colocated earthquakes, whereas small events located in between template earthquakes may remain undetected.

The fault parallel and fault perpendicular cross-sections in Figure 6C show the events' depth distribution. The seismicity is enhanced in the lower half of the seismogenic zone: 7-15 km along the northern strand, and even deeper than 15 km around the Akyazi fault, and 5-10 km depth along the southern strand. The main exception to that depth distribution are the earthquakes at the western side of Lake Sapanca, with hypocenters clustered around 5 km depth. The Lake Sapanca W. cross-section (see Figure 6C) shows that this shallow seismicity seems restricted to the southern side of the fault, namely the Armutlu Bloc.

The map views and cross-sections in Figure 6 suggest a narrower deformation zone in the north where seismicity is mostly distributed within 5-10 km of the main fault trace, whereas we observe a wider deformation zone along the southern strand with seismicity distributed within 15-20 km of the fault trace. We emphasize that the detected microseismicity illuminates the deformation zone associated with the NAFZ rather than the main fault itself. The Sapanca-Akyazi and Akyazi fault perpendicular cross-sections could indicate a north dipping deformation zone with a 60° dip angle in the middle of the Sapanca-Akyazi segment, and 85° near the Akyazi fault. However, these trends are weak and hypocenters mostly show horizontal alignments. Identifying a global dip direction of the deformation zone along the southern strand is equally ambiguous. In the east, one could either identify slightly south dipping structures ($\sim 85^\circ$) or more strongly north dipping structures ($\sim 70^\circ$).

We present the temporal distribution of the seismicity in Figure 7. The recurrence times are given against their detection times for each of the nine cross-sections introduced above. The recurrence time is the time interval between two consecutive co-located earthquakes. In practice, recurrence times are computed as the time intervals between consecutive events detected by a same template. The most striking feature of Figure 7 is the organization of some earthquake sequences into bursts of seismicity with recurrence times spanning many orders of magnitude. These sequences are time clustered (see Section 3.3). These bursts are usually associated with sequences of foreshocks-mainshock-aftershocks, although in general earthquake sequences can have no clear mainshock (that is, an event of magnitude larger than all other events of the sequence) and still exhibit a strong burst-like behavior. The seismicity at the eastern end of Lake Sapanca and near

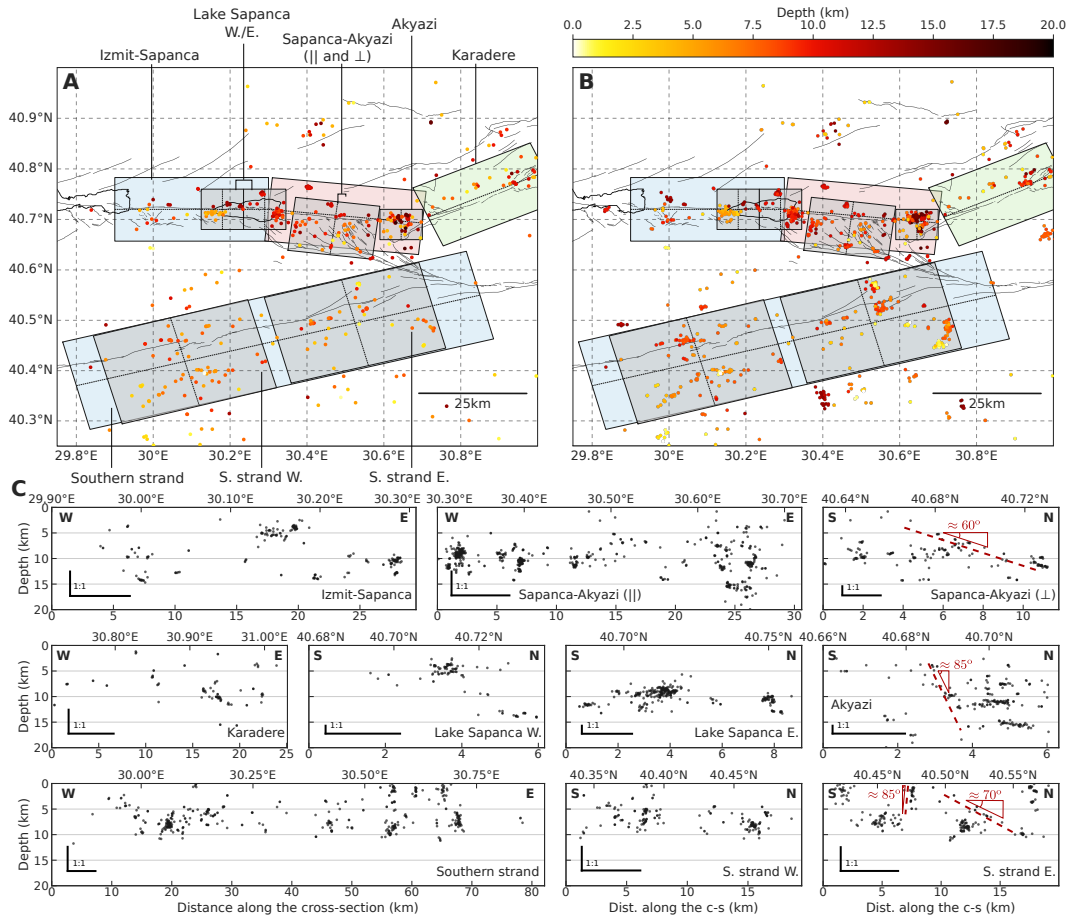


Figure 6. Earthquakes in the North Anatolian Fault Zone. **A:** Locations of the template earthquakes with color coded depths. We define nine subregions along the different segments of the fault. Only in this figure the Sapanca-Akyazi region is subdivided into a fault parallel and a fault perpendicular sections. The thin black dotted lines inside each colored box define either fault parallel or fault perpendicular cross-sections (see bottom panels, C). The color shading of each box is only to help distinguish between them. **B:** Earthquake hypocenters successfully relocated with the double-difference method and color coded by depth. Events for which relocation was not successful were attributed the template location. **C:** Depth cross-sections of the different areas introduced above. The earthquake locations contained in the boxes are projected onto the boxes' central axis. The bottom x-axes are distances along the cross-section axes in kilometers, and the top x-axes are the geographic coordinates relevant to each cross-section (either longitude or latitude). Note that the aspect ratio across cross-sections varies. The 1:1 aspect ratio is drawn in the lower left corner of each cross-section. The dashed red lines and angles are given for reference but are not our take-away message.

411 Akyazi is almost exclusively organized into such sequences of burst-like seismicity, whereas
 412 the southern strand hosts much less of these burst-like episodes. Figure 7 also reports
 413 the local magnitudes (see Section 3.1.5). The Sapanca-Akyazi segment and its vicinity is
 414 the most active region with the largest magnitude events observed during the study per-
 415 iod. Among the nine $M_L \gtrsim 3$ natural earthquakes we detected, three occurred near
 416 each other, close to the city of Serdivan, including the largest event of the study: the 2012-
 417 07-07 $M_L 4.1$ Serdivan earthquake (30.404°E/40.763°N/11.3 km). The area around the Akyazi

418 fault also produced four $M_L > 3$ earthquakes, whereas earthquakes near Lake Sapanca
 419 did not exceed $M_L = 3$.

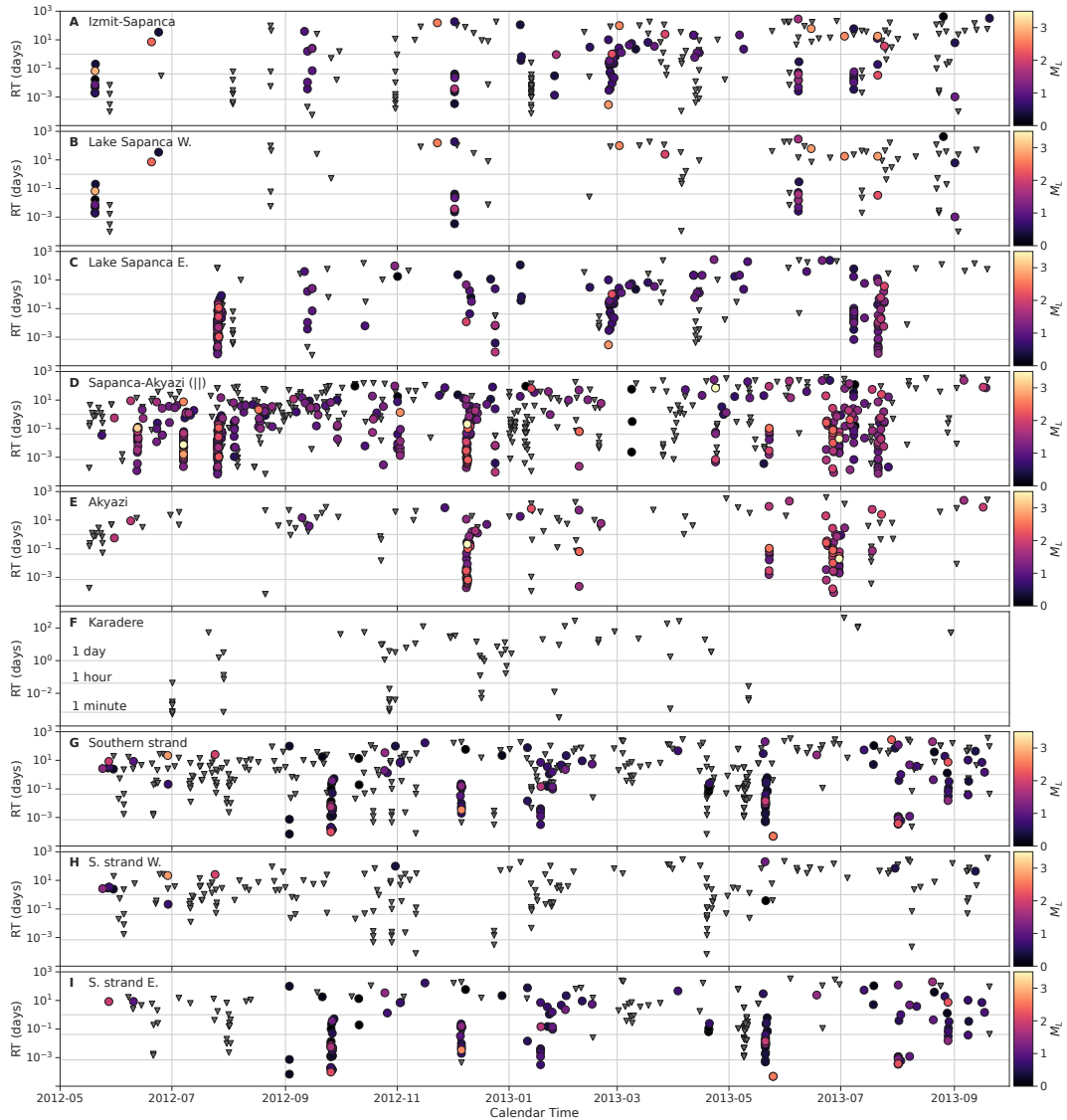


Figure 7. Time evolution of the earthquake recurrence times for different subsets of the earthquake catalog (refer to Figure 6 for the name of the areas). The recurrence time is the time between two consecutive events detected by a same template. Note that the y-axis is in log scale and that some seismic episodes span many orders of magnitude of recurrence time. These episodes are characteristic of burst-like, or cascade activity (see text). The color scale indicates the local magnitude, and inverted grey triangles are events for which no reliable estimates were obtained.

4.1.3 Comparison with Past Seismicity

420
 421 We combined different earthquake catalogs to compare the 2012-2013 detected
 422 seismicity with the pre-Izmit, Izmit-Düzce, and early post-Düzce seismicity (Bulut et al.,
 423 2007; Ickrath et al., 2015; Bohnhoff et al., 2016, and see Figure 8). We note that the Izmit-
 424 Düzce earthquake catalog is more complete in the west (around the Izmit-Sapanca seg-
 425 ment) than the pre-Izmit and early post-Düzce catalogs due to the higher number of sta-

426 tions used in this time period (see, e.g. Ickrath et al., 2015, and Figure 8B). It is also worth
 427 mentioning that these three catalogs show both natural and mining-related seismicity whereas
 428 we have discarded the man-made seismicity to the best of our ability (see Section 3.1.6).
 429 During these three time periods, the (moment) magnitudes of completeness of these cat-
 430 alogs are $M_c = 1.56, 1.69,$ and $1.44,$ respectively, and few $M_w < 1$ earthquakes are re-
 431 ported (see Figure S6). Using our M_w - M_L calibration to convert our local magnitudes to
 432 effective moment magnitudes, we obtained $M_c = 1.18$ and 27% of the earthquakes con-
 433 tributing to the frequency-magnitude distribution have $M_w < 1$ (see Figure S6D). There-
 434 fore, also recalling that most of the detected events are too small to be characterized by
 435 their magnitude, our catalog reports smaller events than the catalogs we compare it with.

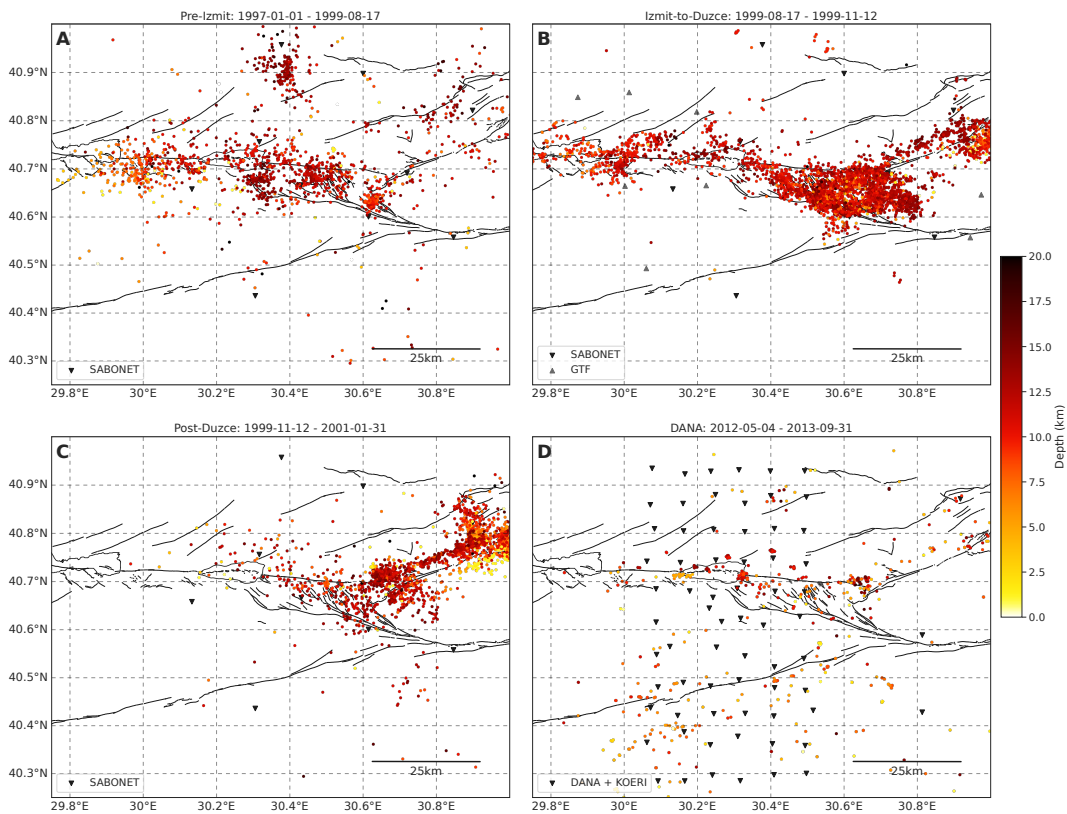


Figure 8. Comparison of the **A:** pre-Izmit, **B:** Izmit-Düzce, the SABONET stations were comple-
 mented by 21 temporary stations from the German Task Force (GTF, grey triangles), **C:** early post-
 Düzce, and **D:** late post-Düzce seismicity. The inverted black triangle are the seismic stations and the
 colored dots are the earthquake locations.

436 The middle sections of the Izmit-Sapanca and Sapanca-Akyazi segments were particu-
 437 larly active seismically before the Izmit earthquake, and some clusters of earthquakes
 438 were observed beneath Lake Sapanca (Figure 8A). The Izmit earthquake is known to have
 439 nucleated near a swarm of seismicity that was active before the M7.4 event (Crampin et
 440 al., 1985; Lovell et al., 1987; Ito et al., 2002). In the three months between the Izmit earth-
 441 quake and the Düzce event, the seismic activity was strongest in the area around the triple
 442 junction between the Sapanca-Akyazi segment, the Karadere segment, and the Mudurnu
 443 fault (Figure 8B). The Izmit hypocentral region remained active and, comparatively, lit-
 444 tle activity was detected near Lake Sapanca. After the Düzce earthquake, most activity
 445 along the Izmit-Sapanca and Sapanca-Akyazi terminated, and seismicity concentrated along
 446 the Karadere segment (Figure 8C). The Akyazi region, where little coseismic slip was ob-
 447 served (Ozalaybey et al., 2002; Bohnhoff et al., 2006, 2008), hosted a cluster of strong

448 activity, possibly driven by the Izmit residual stresses. Note that no seismicity was de-
 449 tected near Lake Sapanca. About 13 years after the Izmit and Düzce earthquakes, we de-
 450 tected the strongest activity at the eastern side of Lake Sapanca, and near the Akyazi fault
 451 (Figure 8D). If not due to the absence of $M < 1$ earthquakes in these catalogs, the lack
 452 of intense seismicity near Lake Sapanca in the early post-Düzce period suggests that faults
 453 near Lake Sapanca did not slip during the afterslip-driven aftershock sequence with Omori-
 454 like decaying seismicity (Perfettini & Avouac, 2004). Moreover, the Omori law predicts
 455 a seismicity rate about four orders of magnitude lower 13 years after the mainshock (using
 456 Omori law parameters from Bayrak & Öztürk, 2004), therefore the seismic activity near
 457 Lake Sapanca should have been high after the Izmit earthquake if the 2012-2013 seis-
 458 micity were to be remnants of aftershocks. The 2012-2013 Lake Sapanca seismicity also
 459 appears much stronger than the pre-Izmit seismicity (Figure 8A).

460 4.2 Observed b-values

461 Computed b-values and magnitudes of completeness (see Section 3.2) are presented
 462 in Figure 9. Of most interest to this study, we see that earthquakes at the eastern side
 463 of Lake Sapanca exhibit higher b-values ($b \approx 1.1$) than earthquakes near the Akyazi fault
 464 ($b \approx 0.8$, see Figure 9D). The magnitude of completeness varies from $M_c \approx 1.3$ near
 465 Akyazi to $M_c \approx 1.0$ near Lake Sapanca. We note that visual checking of the frequency-
 466 magnitude distributions showed that, in general, they follow the Gutenberg-Richter law
 467 well, except for the Serdivan earthquakes where a peak around $M_L \approx 2.5$ can be ob-
 468 served. The significance of the b-value difference between the eastern Lake Sapanca and
 469 Akyazi was assessed by applying the statistical test described in (Utsu, 1966) and we found
 470 that the difference was significant at the 96% confidence level (see Text S1.7).

471 4.3 Observed Temporal Clustering

472 We characterized temporal clustering as a function of space (see Figure 10) follow-
 473 ing the method described in Section 3.3. The strongest temporal clustering (fractal di-
 474 mension $D > 0.20$) is observed on the eastern side of Lake Sapanca, beneath the so-
 475 called Rangefront trace. Other areas of strong activity, like the Serdivan earthquakes (around
 476 $30.404^\circ\text{E}/40.763^\circ\text{N}$) and the Akyazi area, only show small-to-moderate temporal cluster-
 477 ing ($D < 0.14$), thus confirming the outstanding character of the eastern Lake Sapanca.
 478 We note that while the temporal organization of recurrence times shown in Figure 7 in-
 479 dicated burst-like seismicity in all of the above mentioned areas, this quantitative anal-
 480 ysis was necessary to distinguish between strongly and moderately time clustered se-
 481 quences. A few other isolated locations exhibit strong temporal clustering, and seem to
 482 be systematically occurring near the bottom of the seismogenic zone (cf. Figure 10C). Com-
 483 paring the cumulative number of detections per template and their fractal dimension shows
 484 that there is no trivial correlation between the two (see Figure 10A vs. B). We note that
 485 we did the same fractal analysis on all templates of the study region and found another
 486 region of strong temporal clustering on the NAFZ, in the eastern Marmara Sea, where
 487 the 1999 Izmit earthquake arrested (see Figure S7).

488 5 Interpretation and Discussion

489 In the present section, we discuss implications of the observed spatial earthquake
 490 distribution for the mechanical state of the NAFZ (Section 5.1), we interpret the b-values
 491 in terms of low and high stresses (Section 5.2), and we explain how temporal clustering
 492 can be related to fault rheology (Section 5.3).

493 5.1 Spatial Distribution of Seismicity

494 Apart from the Karadere segment, the seismicity is taking place off the main fault
 495 on a complex network of secondary faults, similarly to the Izmit-Düzce aftershocks (e.g.

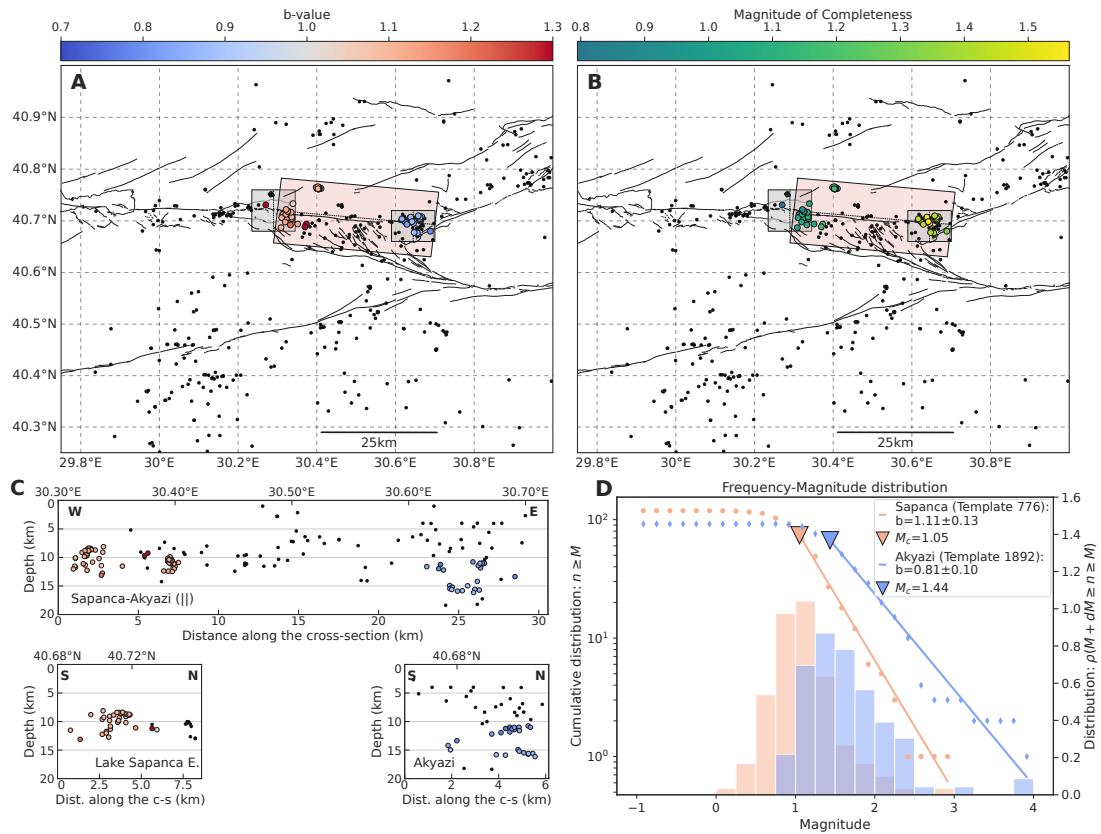


Figure 9. **A:** Map view of template earthquakes with color coded Gutenberg-Richter b -value. Smaller black dots are event families for which we could not compute moment magnitudes (see text). **B:** Map view of template earthquakes with color coded magnitude of completeness. In both top panels, the shaded areas refer to the regions introduced in Figure 6. **C:** Template earthquakes with color coded b -value on fault parallel and fault perpendicular cross-sections. Hypocenters are projected along the dotted axes shown on the map view. **D:** Estimation of the b -value and its uncertainties for two earthquake populations near Lake Sapanca (red, $b \approx 1.1$) and near Akyazi (blue, $b \approx 0.8$). Cumulative (scatter plot) and non-cumulative (histogram) frequency-magnitude distributions. The dashed curves are the kernel density estimate of the non-cumulative probability density functions (pdf). The mode of the pdf is used as the magnitude of completeness (maximum curvature method). The b -value is computed with the maximum likelihood estimate (MLE, Equation (6)).

496 Ozalaybey et al., 2002; Bulut et al., 2007, and see Figure 6). This feature is in stark contrast
 497 with the simplicity of the Izmit and Düzce earthquakes, which occurred on simple
 498 fault segments (Barka et al., 2002; Langridge et al., 2002). Off-fault seismicity has also
 499 been observed to be a characteristic of fault zones early in their seismic cycle (Ben-Zion
 500 & Zaliapin, 2020) and might be due to off-fault, distributed deformation contributing to
 501 accommodate slip deficits resulting from heterogeneous slip along the fault (Dolan & Har-
 502 avitch, 2014).

503 Shallow creep has been observed along the Izmit-Sapanca and the Sapanca-Akyazi
 504 segments (e.g. Çakir et al., 2012; Hussain et al., 2016; Aslan et al., 2019). The creep rates
 505 and creep along the Izmit rupture have evolved with time (e.g. Bürgmann et al.,
 506 2002). Aslan et al. (2019) use 2011-2017 InSAR data and 2014-2016 GPS data and, thus,
 507 is the closest study to ours in time. The authors' model shows shallow creep down to 5 km
 508 along the Izmit-Sapanca segment and down to 2 km at the western end of the Sapanca-

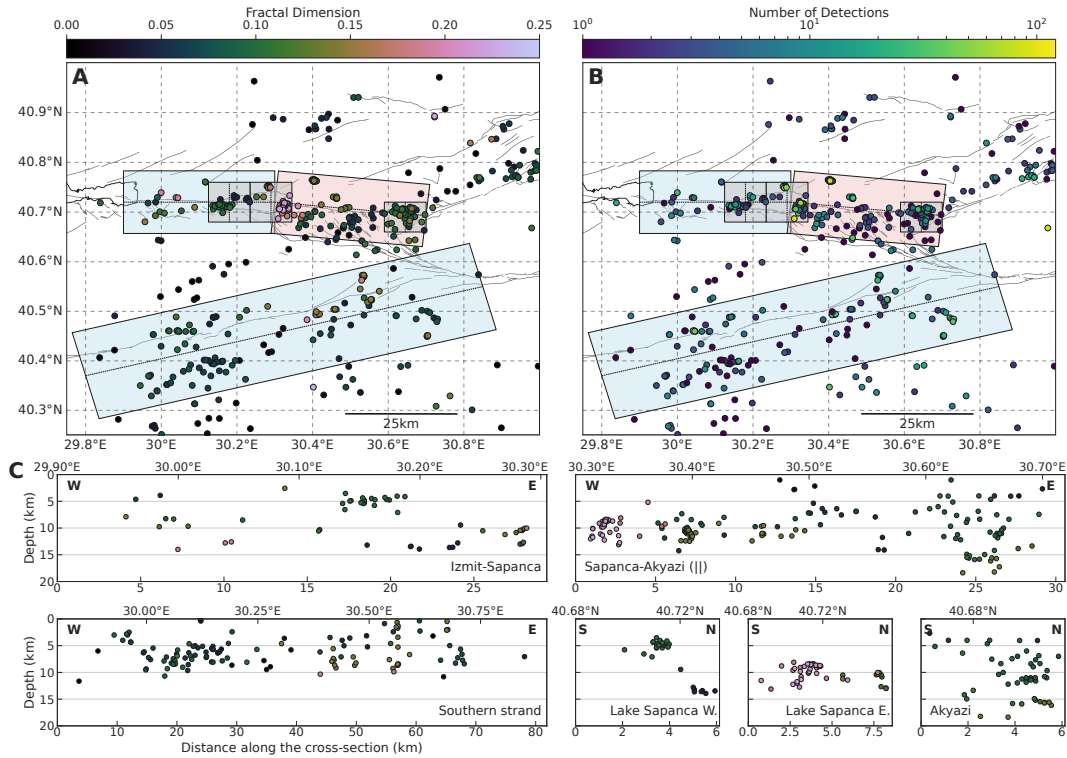


Figure 10. **A:** Map view of template earthquakes with color coded fractal dimension (*cf.* Equation (8)) showing the strength of temporal clustering. **B:** Map view of template earthquakes with color coded cumulative number of detections. In both top panels, the shaded areas refer to the regions introduced in Figure 6. **C:** Template earthquakes with color coded fractal dimension on fault parallel and fault perpendicular cross-sections. Hypocenters are projected along the dotted axes shown on the map view. High fractal dimensions mean strongly time clustered activity (*i.e.* past events strongly influence the timings of future events).

509 Akyazi segment. Such shallow creep should drive microseismicity in the vicinity of the
 510 creeping fault sections (*e.g.* Lohman & McGuire, 2007). The depth cross-sections (Fig-
 511 ure 6C) only show shallow seismicity at the western Lake Sapanca (≈ 5 km depth). Although
 512 these depths are consistent with the creep depth given in Aslan et al. (2019), a direct causal-
 513 ity link to the shallow creep is not straightforward because it is taking place off-fault (Fig-
 514 ure 6B). Seismicity along the Sapanca-Akyazi segment do not support creep-driven activ-
 515 ity at shallow depths (≈ 2 km). However, hypocenters suggest that, at the time of the
 516 study, the base of the seismogenic zone is around 10-15 km, which is in good agreement
 517 with Aslan et al. (2019).

518 Comparing our catalog with the seismicity in the past (see Section 4.1.3) showed
 519 that the eastern Lake Sapanca did not appear to be a particularly active area, either be-
 520 fore or right after the Izmit earthquake. However, this comparison relies on catalogs made
 521 with different methods and station coverage, and, consequently, different magnitudes
 522 of completeness. The seismic activity at the eastern Lake Sapanca may be a permanent
 523 feature of the step-over that can only be observed with low magnitude of completeness
 524 catalogs ($M_c \lesssim 1.0$). We further discuss in Section 5.4 whether the seismicity at the east-
 525 ern Lake Sapanca is a new feature of the fault zone caused by the post-Izmit deforma-
 526 tion or is a constant phenomenon that could not be observed in such detail in the past.
 527 Variations in seismicity along the southern strand are harder to interpret because the lack

528 of earthquakes in previous catalogs (see Figure 8) is partly due to the absence of stations
 529 in the past.

530 5.2 Gutenberg-Richter b -value

531 Laboratory experiments have shown that the b -value seems to be controlled by the
 532 state of stress, specifically that b decreases with increasing differential stress (e.g. C. H. Scholz,
 533 1968; Amitrano, 2003). Decreasing b -value with depth (Mori & Abercrombie, 1997; Wiemer
 534 & Wyss, 1997) and high b -value along creeping sections (e.g. Amelung & King, 1997; Wiemer
 535 & Wyss, 1997) also support the negative correlation of b with stress. Thus, the b -value
 536 can be used as a stressmeter.

537 Our results (Figure 9) show a clear difference in b -values between the eastern Lake
 538 Sapanca ($b \approx 1.1$) and the Akyazi ($b \approx 0.8$) seismicity. We recall that this difference is
 539 significant at the 96% confidence level (see Section 4.2). We interpret the higher b -values
 540 at Lake Sapanca as an indication of low background stresses, while we interpret the lower
 541 b -values at Akyazi as indicating high background stresses. Low stress at the eastern Lake
 542 Sapanca suggests that aseismic slip might play a role in driving the seismicity, implying
 543 that, there, faults have weak sections. High stress near Akyazi can be understood as re-
 544 sulting from the stress concentration that occurred during the Izmit earthquake, when
 545 little co-seismic slip occurred along the Akyazi fault and the Akyazi gap.

546 5.3 Temporal Clustering, Earthquake Interactions, and Fault Mechanical Proper- 547 ties

548 Strongly time clustered seismicity with a wide range of recurrence times, as presented
 549 in Section 4.3, cannot be explained only by fluctuations of the background seismicity rate,
 550 for example due to the injection of fluids at depth. Indeed, a Poisson point process with
 551 a transient increased rate only shifts the distribution of recurrence times towards shorter
 552 times but does not widen the distribution and does not have a large fractal dimension (see
 553 Figure S8). Temporal clustering, that is, cascading of events, emerges when different faults
 554 or sections of a fault interact (e.g. Burridge & Knopoff, 1967; Marsan & Lengline, 2008;
 555 Fischer & Hainzl, 2021). Earthquakes can trigger each other due to the static stress changes
 556 induced by the co- and postseismic displacements (e.g. King & Cocco, 2001), but also due
 557 to the dynamic stress changes induced by the elastic waves radiated by the rapid coseis-
 558 mic motions (e.g. Fan & Shearer, 2016). Furthermore, because of the stress redistribu-
 559 tion following any slip motion (not necessarily at seismic speeds), interaction can occur
 560 between a seismogenic asperity and its creeping surroundings: accelerated creep (e.g. af-
 561 terslip) increases the stressing rate on the asperity (e.g. Cattania, 2019; Cattania & Segall,
 562 2021). In realistic, complex conditions where seismic and aseismic slip co-occurs on short
 563 length scales (e.g. Collettini et al., 2011), numerical models show that both co-seismic and
 564 creep mediated stress changes are important factors controlling the clustering of earth-
 565 quakes (Dublanche et al., 2013; Cattania & Segall, 2021). The contribution of creep me-
 566 diated stress transfers to temporal clustering might even be more important than static
 567 stress changes due to the breaking of asperities (Dublanche, 2019). In fact, this means
 568 that both seismic and aseismic events can cluster in time, but that earthquake catalogs
 569 only capture the seismic signature of temporal clustering. Effectively, these interacting
 570 stress fields result in a clock advance or delay in the cycle of the earthquake sources (e.g.
 571 Harris et al., 1995; Gomberg et al., 1998) and thus in non-random earthquake sequences.

572 Figure 11 sketches different earthquake interaction scenarios explaining tempo-
 573 ral clustering: in a locked fault Figure 11A, and with creep mediated stress transfers Fig-
 574 ure 11B. Note that remote creep acting on a sparse asperity population (Figure 11C) would
 575 produce Poissonian seismicity (e.g. Lohman & McGuire, 2007). Thus, areas of strong tem-
 576 poral clustering (see Figure 10) indicate faults with intrinsic properties: heterogeneous
 577 rheology resulting in juxtaposed seismic and aseismic slip, and rough or densely fractured
 578 fault zone providing many seismogenic asperities. These properties enhance interaction-

579 driven seismicity, that is, driven by the redistributed stresses of past events. However,
 580 the long time-scale behavior of clustered seismicity may be modulated by time-dependent
 581 remote forcing.

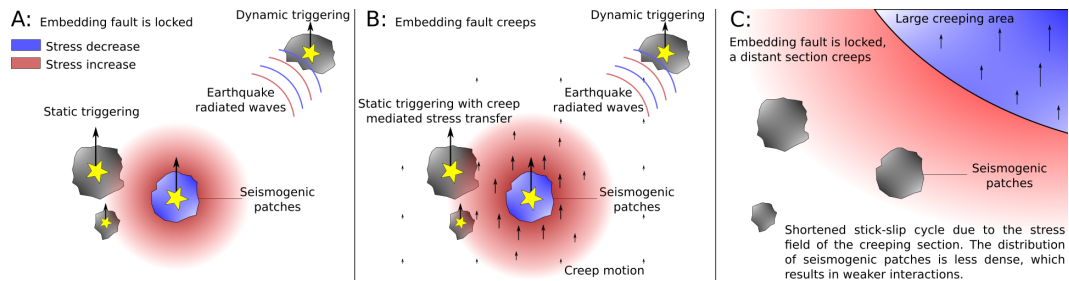


Figure 11. Sketch of different earthquake interaction scenarios. **A:** Seismogenic asperities embedded in a locked fault. **B:** Seismogenic asperities embedded in a creeping fault. In **A** and **B**, the color shows the stress change due to rupture of the seismogenic patch. The triggered ruptures occur with some delay. **C:** Seismogenic asperities embedded in a locked fault, but stressed by a remote creeping section of the fault. The asperities are not close enough to the creeping patch to strongly interact via static stress changes. The spatial configuration of asperities does not promote strong interactions.

582 Where rheology transitions from brittle to ductile, for example at the base of the
 583 seismogenic zone, faults are likely to host both unstable, seismic slip and stable, aseis-
 584 mic slip (C. H. Scholz, 1998; Skarbek et al., 2012). Therefore, seismicity near the bottom
 585 of the seismogenic zone would be expected to display temporal clustering because, there,
 586 interacting asperities are likely to be embedded in a creeping fault (cf. Figure 11B, Dublanchet
 587 et al., 2013). We investigated the relationship between temporal clustering and the prox-
 588 imity to the bottom of the seismogenic zone to elucidate the role of fault stability in our
 589 observations (i.e. scenario Figure 11A vs. 11B). The results, in Figure 12, indicate that,
 590 as expected, seismicity tends to get more time clustered as it gets closer to the brittle-
 591 ductile transition and that strong clustering almost always happens at the bottom of the
 592 seismogenic zone. Exceptions are at the western side of Lake Sapanca (Figure 12B) where
 593 results might be biased due to the absence of significant seismicity at depth, and along
 594 the Karadere segment (Figure 12F) where large source-receiver distances yield poor hypocen-
 595 tral depth resolution and thus low confidence results.

596 We also investigated a possible correlation between the proximity to the brittle-ductile
 597 transition and the density of seismic sources, which could as well explain the increase in
 598 temporal clustering. We took the average inter-event distance within neighboring earth-
 599 quake subcatalogs as a proxy for asperity density. We note that this measure of asper-
 600 ity density is imperfect because a single asperity can break repeatedly. The smaller num-
 601 ber of detected earthquakes along the southern strand might also be insufficient to com-
 602 pute a meaningful average inter-event distance. We do not observe a clear systematic
 603 increase in asperity density with decreasing distance from the bottom of the seismogenic
 604 zone, but the observational limits mentioned above prevent us from drawing definite con-
 605 clusions. Figure 12 rather shows that both the proximity to the brittle-ductile transition
 606 and a large event density favor temporal clustering. Our observations therefore support
 607 that dense asperity populations along with creep mediated stress transfers do promote
 608 strong temporal clustering (cf. Figure 11B, Dublanchet et al., 2013). Thus, this study sug-
 609 gests that faults at the eastern side of Lake Sapanca are in heterogeneous stability regimes
 610 allowing unstable (seismic) and stable (aseismic) slip.

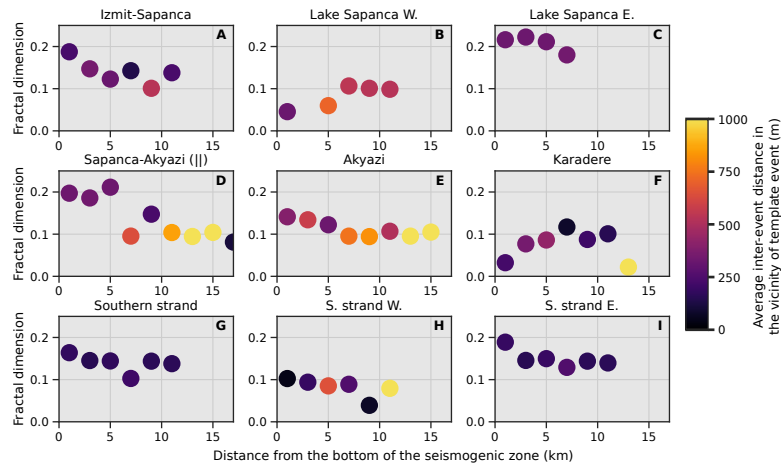


Figure 12. Clustering vs. depth vs. event density. Inside each region, templates are binned per distance from the bottom of the seismogenic zone and the fractal dimension is averaged among the 10% largest values, resulting in a "soft" maximum of each bin. The location of the bottom of the seismogenic zone is approximated by the depth of the locally deepest template. Dots are colored according to the average inter-event distance within the neighboring earthquake subcatalogs; this is a proxy for asperity density. Darker colors mean higher density. Strongest clustering tends to occur at the bottom of the seismogenic zone, *i.e.* at the transition zone between unstable (brittle) and stable (ductile) sliding.

611

5.4 Implications for the Lake Sapanca Step-Over

612

613

614

615

616

617

618

In summary, the Gutenberg-Richter b -values (see Section 5.2) and temporal clustering (see Section 5.3) point to the role of different rheological properties in producing earthquakes between the two sides of Lake Sapanca. At the western side, the shallow active sections seem incapable of producing strongly time clustered seismicity. At the eastern side, the depth distribution, the strong temporal clustering (Figure 10C), and the relatively high b -values (Figure 9) suggest that thin along-dip fault sections slip in a mixed seismic and aseismic mode.

619

620

621

622

623

624

625

626

627

628

629

630

631

632

633

634

635

636

637

Heterogeneous faults near the brittle-ductile transition have stable and unstable sections (e.g. Collettini et al., 2011). Weakly unstable sections may produce transient episodes of slow slip (e.g. Bürgmann, 2018). The temporal distribution of earthquakes at the eastern Lake Sapanca (see Figure 7C) suggests that faults are slipping during intermittent episodes of deformation. Thus, the weakest sections of the faults at the eastern Lake Sapanca might be intermittently driven to slowly slip and, in turn, activate the seismogenic asperities (Skarbak et al., 2012; Cattania & Segall, 2021). The lack of seismicity along the up-dip sections suggests they are either fully locked or fully creeping, but there is no evidence for such a large creeping section in geodetic data (e.g. Aslan et al., 2019). Geologic data suggest that the so-called Sapanca Complex, constituted of weak serpentinites and strong metabasites (Akbayram et al., 2013, and references therein), might reach the southeastern side of Lake Sapanca at depth where we observe the highly clustered seismicity. Such lithology is consistent with the scenario of strong asperities embedded in a weak, stable fault. How much seismic moment is released through (partial) aseismic slip during these episodes of strong microseismicity remains an open question.

Whether these intermittent episodes of deformation are a permanent feature of Lake Sapanca or result from the mechanical changes that faults underwent because of co- and post-seismic stress changes is hard to elucidate entirely since our comparison with the past seismicity relies on unequal catalogs (see Section 4.1.3). However, we know from

geodetic data that north-south extension around the Lake Sapanca step-over accelerated considerably following the Izmit earthquake (Ergintav et al., 2009; Hearn et al., 2009). Stress analyses have also shown that the NAFZ weakened after the Izmit-Düzce earthquake sequence (e.g. Pinar et al., 2010; Ickrath et al., 2015). Given that deformation in the step-over is faster than before the Izmit earthquake, (micro)seismicity should also be stronger. Early post Izmit-Düzce seismicity (before early 2001) is either lacking from the catalogs due to insufficient detection capability, or the increase of seismicity occurred later due to postseismic relaxation processes such as enhanced slip rates below seismogenic depths.

The postseismic response of at least two releasing step-overs of the NAFZ, Lake Sapanca and another one in the eastern Marmara Sea, has been shown to produce substantial north-south extension following the Izmit earthquake (Ergintav et al., 2009; Hearn et al., 2009). Ergintav et al. (2009) have shown that models of postseismic slip on the main fault do not account well for the north-south extension in these two step-overs, in particular after the first three years. We further compared these step-overs by extending our temporal clustering analysis further along the NAFZ and found that the eastern Marmara Sea was also hosting clustered seismicity at the eastern termination of the Princes Islands segment (cf. Figure S7). Large earthquake location uncertainties prevented us from carrying the same detailed study but this section has been identified as an area of high b -value (Raub et al., 2017). We can hypothesize that Lake Sapanca and the eastern Marmara Sea behave similarly. In both cases, fault heterogeneities, and perhaps their stress history, could explain an hybrid seismic and aseismic slip regime (Collettini et al., 2011). As to how much slip is accommodated seismically vs. aseismically and whether the aseismic part is related to the deformation missing from the current models has to be addressed by the means of geodesy.

6 Concluding Remarks

We found that the patterns of seismicity have changed after the Izmit-Düzce earthquake sequence (see Section 4.1.3). We observed two regions of high seismicity, the Akyazi fault and the Lake Sapanca step-over (Section 4.1), with different statistical properties (see Sections 4.2 and 4.3). Our interpretation is that the Akyazi seismicity was driven by the high residual stresses left by the absence of co-seismic during the 1999 Izmit earthquake whereas the Lake Sapanca seismicity was caused by mixed seismic and aseismic slip on heterogeneous faults at the brittle-ductile transition (Section 5).

Our study emphasizes the important role of secondary structures in the late post-seismic stage of the NAFZ, and possibly through the interseismic phase. The structural complexity of these structures appears in stark contrast to the relatively simple co-seismic dynamics of the Izmit earthquake (rupture on almost straight and vertical fault segments). Given that the north-south extension across the Lake Sapanca step-over accelerated following the Izmit earthquake, we question whether the proposed seismic-aseismic heterogeneous slip regime could be related to this deformation (see Section 5.4). The seismicity supports, but not prove, the possibility of slow slip in the step-over. We suggested that the releasing step-over in the Marmara Sea, with similar temporal clustering and accelerated extension following the Izmit earthquake, could behave analogously to the Lake Sapanca step-over. The present study does not provide the means to relate the observed surface deformation to slip on specific faults, but it does encourage the search for slow slip on normal faults in these step-overs. Finally, our study emphasizes that slip may not always happen in well separated seismic and aseismic sections but, instead, may happen over complex, intricate unstable and stable domains.

7 Data and Resources

The earthquake catalog is available at the Zenodo data set repository (DOI: 10.5281/zenodo.6362973). We used the version 1.0.1 of our BPFM Python package for earthquake

689 detection and location, which is stored at <https://doi.org/10.5281/zenodo.6780316>
690 (last accessed December 2021). The last version is maintained on Github at [https://github](https://github.com/ebeauce/Seismic_BPMF)
691 [.com/ebeauce/Seismic_BPMF](https://github.com/ebeauce/Seismic_BPMF).

692 The topographic data used for the maps were taken from the Shuttle Radar Topo-
693 graphic Mission (SRTM) 90-m database ([https://cgiarcsi.community/data/srtm-90m-](https://cgiarcsi.community/data/srtm-90m-digital-elevation-database-v4-1/)
694 [digital-elevation-database-v4-1/](https://cgiarcsi.community/data/srtm-90m-digital-elevation-database-v4-1/), last accessed December 2021). The maps were
695 made with the Cartopy Python library (version 0.18.0, last accessed December 2021, Met
696 Office, 2010 - 2015). The seismic data were recorded by the temporary array DANA (DANA
697 , 2012, DOI: https://doi.org/10.7914/SN/YH_2012) and by the permanent KOERI sta-
698 tions (Kandilli Observatory And Earthquake Research Institute, Boğaziçi University, 1971,
699 DOI: <https://doi.org/10.7914/SN/KO>).

700 **Acknowledgements**

701 The authors thank the editors and two anonymous reviewers for helping improve
702 the study and the manuscript. This project has received funding from the European Re-
703 search Council (ERC) under the European Union's Horizon H2020 research and innova-
704 tion program (grant agreement No 742335, F-IMAGE). E.B. was also supported by funds
705 associated with Robert D. van der Hilst's Schlumberger chair.

References

- 706
707 Akbayram, K., Okay, A. I., & Satır, M. (2013). Early cretaceous closure of the intra-
708 pontide ocean in western pontides (northwestern turkey). *Journal of Geodynam-*
709 *ics*, 65, 38–55.
- 710 Aki, K. (1965). Maximum likelihood estimate of b in the formula $\log n = a - bm$ and its
711 confidence limits. *Bull. Earthq. Res. Inst., Tokyo Univ.*, 43, 237–239.
- 712 Amelung, F., & King, G. (1997). Earthquake scaling laws for creeping and non-
713 creeping faults. *Geophysical research letters*, 24(5), 507–510.
- 714 Amitrano, D. (2003). Brittle-ductile transition and associated seismicity: Experimen-
715 tal and numerical studies and relationship with the b value. *Journal of Geophysi-*
716 *cal Research: Solid Earth*, 108(B1).
- 717 Aslan, G., Lasserre, C., Cakir, Z., Ergintav, S., Özarpacı, S., Dogan, U., ... Renard, F.
718 (2019). Shallow creep along the 1999 Izmit earthquake rupture (Turkey) from
719 GPS and high temporal resolution interferometric synthetic aperture radar data
720 (2011–2017). *Journal of Geophysical Research: Solid Earth*, 124(2), 2218–2236.
- 721 Barka, A., Akyuz, H., Altunel, E., Sunal, G., Cakir, Z., Dikbas, A., ... others (2002). The
722 surface rupture and slip distribution of the 17 august 1999 Izmit earthquake (m
723 7.4), North Anatolian fault. *Bulletin of the Seismological Society of America*, 92(1),
724 43–60.
- 725 Bayrak, Y., & Öztürk, S. (2004). Spatial and temporal variations of the aftershock
726 sequences of the 1999 izmit and düzce earthquakes. *Earth, planets and space*,
727 56(10), 933–944.
- 728 Beaucé, E., Frank, W. B., Paul, A., Campillo, M., & van der Hilst, R. D. (2019). System-
729 atic detection of clustered seismicity beneath the Southwestern Alps. *Journal of*
730 *Geophysical Research: Solid Earth*, 124(11), 11531–11548.
- 731 Beaucé, E., Frank, W. B., & Romanenko, A. (2018). Fast matched filter (FMF): An ef-
732 ficient seismic matched-filter search for both CPU and GPU architectures. *Seis-*
733 *mological Research Letters*, 89(1), 165–172.
- 734 Ben-Zion, Y., & Zaliapin, I. (2020). Localization and coalescence of seismicity before
735 large earthquakes. *Geophysical Journal International*, 223(1), 561–583.
- 736 Bohnhoff, M., Bulut, F., Görgün, E., Milkereit, C., & Dresen, G. (2008). Seismotectonic
737 setting at the north anatolian fault zone after the 1999 mw= 7.4 izmit earth-
738 quake based on high-resolution aftershock locations. *Advances in Geosciences*,
739 14, 85–92.
- 740 Bohnhoff, M., Grosser, H., & Dresen, G. (2006). Strain partitioning and stress ro-
741 tation at the North Anatolian fault zone from aftershock focal mechanisms of
742 the 1999 Izmit m w= 7.4 earthquake. *Geophysical Journal International*, 166(1),
743 373–385.
- 744 Bohnhoff, M., Ickrath, M., & Dresen, G. (2016). Seismicity distribution in conjunction
745 with spatiotemporal variations of coseismic slip and postseismic creep along
746 the combined 1999 izmit-düzce rupture. *Tectonophysics*, 686, 132–145.
- 747 Bouchon, M., Bouin, M.-P., Karabulut, H., Toksöz, M. N., Dietrich, M., & Rosakis, A. J.
748 (2001). How fast is rupture during an earthquake? new insights from the 1999
749 Turkey earthquakes. *Geophysical Research Letters*, 28(14), 2723–2726.
- 750 Bouchon, M., Karabulut, H., Aktar, M., Özalaybey, S., Schmittbuhl, J., & Bouin, M.-P.
751 (2011). Extended nucleation of the 1999 mw 7.6 Izmit earthquake. *science*,
752 331(6019), 877–880.
- 753 Brune, J. N. (1970). Tectonic stress and the spectra of seismic shear waves from
754 earthquakes. *Journal of geophysical research*, 75(26), 4997–5009.
- 755 Bulut, F., Bohnhoff, M., Aktar, M., & Dresen, G. (2007). Characterization of
756 aftershock-fault plane orientations of the 1999 izmit (turkey) earthquake us-
757 ing high-resolution aftershock locations. *Geophysical Research Letters*, 34(20).
- 758 Bürgmann, R. (2018). The geophysics, geology and mechanics of slow fault slip. *Earth*
759 *and Planetary Science Letters*, 495, 112–134.

- 760 Bürgmann, R., Ergintav, S., Segall, P., Hearn, E. H., McClusky, S., Reilinger, R. E., ...
 761 Zschau, J. (2002). Time-dependent distributed afterslip on and deep below the
 762 izmit earthquake rupture. *Bulletin of the Seismological Society of America*, 92(1),
 763 126–137.
- 764 Burridge, R., & Knopoff, L. (1967). Model and theoretical seismicity. *Bulletin of the*
 765 *seismological society of america*, 57(3), 341–371.
- 766 Cakir, Z., Chabalier, J.-B. d., Armijo, R., Meyer, B., Barka, A., & Peltzer, G. (2003). Co-
 767 seismic and early post-seismic slip associated with the 1999 izmit earthquake
 768 (turkey), from sar interferometry and tectonic field observations. *Geophysical*
 769 *Journal International*, 155(1), 93–110.
- 770 Çakir, Z., Ergintav, S., Özener, H., Dogan, U., Akoglu, A. M., Meghraoui, M., &
 771 Reilinger, R. (2012). Onset of aseismic creep on major strike-slip faults. *Ge-*
 772 *ology*, 40(12), 1115–1118.
- 773 Cattania, C. (2019). Complex earthquake sequences on simple faults. *Geophysical Re-*
 774 *search Letters*, 46(17-18), 10384–10393.
- 775 Cattania, C., & Segall, P. (2021). Precursory slow slip and foreshocks on rough faults.
 776 *Journal of Geophysical Research: Solid Earth*, 126(4), e2020JB020430.
- 777 Collettini, C., Niemeijer, A., Viti, C., Smith, S. A., & Marone, C. (2011). Fault struc-
 778 ture, frictional properties and mixed-mode fault slip behavior. *Earth and Plane-*
 779 *tary Science Letters*, 311(3-4), 316–327.
- 780 Crampin, S., Evans, R., & Üçer, S. B. (1985). Analysis of records of local earthquakes:
 781 the turkish dilatancy projects (tdp1 and tdp2). *Geophysical Journal International*,
 782 83(1), 1–16.
- 783 DANA . (2012). *Dense array for north anatolia*. International Federation of Digital Seis-
 784 mograph Networks. Retrieved from [http://www.fdsn.org/doi/10.7914/SN/](http://www.fdsn.org/doi/10.7914/SN/YH_2012)
 785 [YH_2012](http://www.fdsn.org/doi/10.7914/SN/YH_2012) doi: 10.7914/SN/YH_2012
- 786 Dolan, J. F., & Haravitch, B. D. (2014). How well do surface slip measurements track
 787 slip at depth in large strike-slip earthquakes? the importance of fault structural
 788 maturity in controlling on-fault slip versus off-fault surface deformation. *Earth*
 789 *and Planetary Science Letters*, 388, 38–47.
- 790 Dublanchet, P. (2019). Scaling and variability of interacting repeating earthquake
 791 sequences controlled by asperity density. *Geophysical Research Letters*, 46(21),
 792 11950–11958.
- 793 Dublanchet, P., Bernard, P., & Favreau, P. (2013). Interactions and triggering in a
 794 3-d rate-and-state asperity model. *Journal of Geophysical Research: Solid Earth*,
 795 118(5), 2225–2245.
- 796 Efron, B., & Tibshirani, R. (1986). Bootstrap methods for standard errors, confidence
 797 intervals, and other measures of statistical accuracy. *Statistical science*, 54–75.
- 798 Ergintav, S., McClusky, S., Hearn, E., Reilinger, R., Cakmak, R., Herring, T., ... Tari, E.
 799 (2009). Seven years of postseismic deformation following the 1999, $m = 7.4$
 800 and $m = 7.2$, izmit-düzce, turkey earthquake sequence. *Journal of Geophysical*
 801 *Research: Solid Earth*, 114(B7).
- 802 Fan, W., & Shearer, P. M. (2016). Local near instantaneously dynamically triggered af-
 803 tershocks of large earthquakes. *Science*, 353(6304), 1133–1136.
- 804 Fischer, T., & Hainzl, S. (2021). The growth of earthquake clusters. *Frontiers in Earth*
 805 *Science*, 9, 79.
- 806 Frank, W., & Shapiro, N. (2014). Automatic detection of low-frequency earthquakes
 807 (lfes) based on a beamformed network response. *Geophysical Journal Interna-*
 808 *tional*, 197(2), 1215–1223.
- 809 Gardner, J., & Knopoff, L. (1974). Is the sequence of earthquakes in Southern Cali-
 810 fornia, with aftershocks removed, Poissonian? *Bulletin of the Seismological Soci-*
 811 *ety of America*, 64(5), 1363–1367.
- 812 Gibbons, S. J., & Ringdal, F. (2006). The detection of low magnitude seismic events
 813 using array-based waveform correlation. *Geophysical Journal International*,
 814 165(1), 149–166.

- 815 Gomberg, J., Beeler, N., Blanpied, M., & Bodin, P. (1998). Earthquake triggering by
816 transient and static deformations. *Journal of Geophysical Research: Solid Earth*,
817 103(B10), 24411–24426.
- 818 Gutenberg, B., & Richter, C. (1941). *Seismicity of the earth* (Vol. 34). Geological Soci-
819 ety of America.
- 820 Harris, R. A., Simpson, R. W., & Reasenber, P. A. (1995). Influence of static stress
821 changes on earthquake locations in southern california. *Nature*, 375(6528),
822 221–224.
- 823 Hearn, E., McClusky, S., Ergintav, S., & Reilinger, R. (2009). Izmit earthquake postseis-
824 mic deformation and dynamics of the north anatolian fault zone. *Journal of Geo-
825 physical Research: Solid Earth*, 114(B8).
- 826 Hussain, E., Wright, T. J., Walters, R. J., Bekaert, D., Hooper, A., & Houseman, G. A.
827 (2016). Geodetic observations of postseismic creep in the decade after the
828 1999 Izmit earthquake, Turkey: Implications for a shallow slip deficit. *Journal of
829 Geophysical Research: Solid Earth*, 121(4), 2980–3001.
- 830 Ickrath, M., Bohnhoff, M., Dresen, G., Martinez-Garzon, P., Bulut, F., Kwiatek, G.,
831 & Germer, O. (2015). Detailed analysis of spatiotemporal variations of the
832 stress field orientation along the izmit-düzce rupture in nw turkey from inver-
833 sion of first-motion polarity data. *Geophysical Journal International*, 202(3),
834 2120–2132.
- 835 Ito, A., Uçer, B., Bariş, Ş., Nakamura, A., Honkura, Y., Kono, T., ... Işıkara, A. M. (2002).
836 Aftershock activity of the 1999 izmit, turkey, earthquake revealed from mi-
837 croearthquake observations. *Bulletin of the Seismological Society of America*,
838 92(1), 418–427.
- 839 Kahraman, M., Cornwell, D. G., Thompson, D. A., Rost, S., Houseman, G. A., Türkelli,
840 N., ... Gülen, L. (2015, Nov). Crustal-scale shear zones and heterogeneous
841 structure beneath the North Anatolian Fault Zone, Turkey, revealed by a
842 high-density seismometer array. *Earth Planet. Sci. Lett.*, 430, 129–139. doi:
843 10.1016/j.epsl.2015.08.014
- 844 Kandilli Observatory And Earthquake Research Institute, Boğaziçi University. (1971).
845 *Bogazici university kandilli observatory and earthquake research institute*. Interna-
846 tional Federation of Digital Seismograph Networks. Retrieved from [http://www](http://www.fdsn.org/doi/10.7914/SN/KO)
847 [.fdsn.org/doi/10.7914/SN/KO](http://www.fdsn.org/doi/10.7914/SN/KO) doi: 10.7914/SN/KO
- 848 Karabulut, H., Schmittbuhl, J., Özalaybey, S., Lengline, O., Kömeç-Mutlu, A., Durand,
849 V., ... Bouin, M. (2011). Evolution of the seismicity in the eastern Marmara
850 Sea a decade before and after the 17 August 1999 Izmit earthquake. *Tectono-
851 physics*, 510(1-2), 17–27.
- 852 Karahan, A. E., Berckhemer, H., & Baier, B. (2001). Crustal structure at the western
853 end of the North Anatolian Fault Zone from deep seismic sounding.
- 854 King, G., & Cocco, M. (2001). Fault interaction by elastic stress changes: New clues
855 from earthquake sequences. In *Advances in geophysics* (Vol. 44, pp. 1–VIII). Else-
856 vier.
- 857 Langridge, R., Stenner, H. D., Fumal, T., Christofferson, S., Rockwell, T., Hartleb, R.,
858 ... Barka, A. (2002). Geometry, slip distribution, and kinematics of surface
859 rupture on the sakarya fault segment during the 17 august 1999 izmit, turkey,
860 earthquake. *Bulletin of the Seismological Society of America*, 92(1), 107–125.
- 861 Lee, H.-K., & Schwarcz, H. P. (1995). Fractal clustering of fault activity in california.
862 *Geology*, 23(4), 377–380.
- 863 Le Pichon, X., & Angelier, J. (1979). The hellenic arc and trench system: a key to the
864 neotectonic evolution of the eastern mediterranean area. *Tectonophysics*, 60(1-
865 2), 1–42.
- 866 Lohman, R., & McGuire, J. (2007). Earthquake swarms driven by aseismic creep in the
867 salton trough, california. *Journal of Geophysical Research: Solid Earth*, 112(B4).
- 868 Lomax, A., Michelini, A., Curtis, A., & Meyers, R. (2009). Earthquake location, direct,
869 global-search methods. *Encyclopedia of complexity and systems science*, 5, 2449–

- 870 2473.
- 871 Lomax, A., Virieux, J., Volant, P., & Berge-Thierry, C. (2000). Probabilistic earth-
872 quake location in 3D and layered models. In *Advances in seismic event location*
873 (pp. 101–134). Springer.
- 874 Lovell, J., Crampin, S., Evans, R., & Üçer, S. B. (1987). Microearthquakes in the tdp
875 swarm, turkey: clustering in space and time. *Geophysical Journal International*,
876 *91*(2), 313–330.
- 877 Lowen, S. B., & Teich, M. C. (2005). *Fractal-based point processes* (Vol. 366). John Wi-
878 ley & Sons.
- 879 Marsan, D., & Lengline, O. (2008). Extending earthquakes' reach through cascading.
880 *Science*, *319*(5866), 1076–1079.
- 881 McClusky, S., Balassanian, S., Barka, A., Demir, C., Ergintav, S., Georgiev, I., ... others
882 (2000). Global positioning system constraints on plate kinematics and dynamics
883 in the eastern mediterranean and caucasus. *Journal of Geophysical Research:*
884 *Solid Earth*, *105*(B3), 5695–5719.
- 885 Meade, B. J., Hager, B. H., McClusky, S. C., Reilinger, R. E., Ergintav, S., Lenk, O., ...
886 Ozener, H. (2002). Estimates of seismic potential in the marmara sea region
887 from block models of secular deformation constrained by global positioning
888 system measurements. *Bulletin of the Seismological Society of America*, *92*(1),
889 208–215.
- 890 Met Office. (2010 - 2015). Cartopy: a cartographic python library with a matplotlib
891 interface [Computer software manual]. Exeter, Devon. Retrieved from [http://](http://scitools.org.uk/cartopy)
892 scitools.org.uk/cartopy
- 893 Moreau, L., Stehly, L., Boué, P., Lu, Y., Larose, E., & Campillo, M. (2017). Improving
894 ambient noise correlation functions with an SVD-based Wiener filter. *Geophys-*
895 *ical Journal International*, *211*(1), 418–426.
- 896 Mori, J., & Abercrombie, R. E. (1997). Depth dependence of earthquake frequency-
897 magnitude distributions in california: Implications for rupture initiation. *Journal*
898 *of Geophysical Research: Solid Earth*, *102*(B7), 15081–15090.
- 899 Ozalaybey, S., Ergin, M., Aktar, M., Tapirdamaz, C., Biçmen, F., & Yörük, A. (2002). The
900 1999 izmit earthquake sequence in turkey: seismological and tectonic aspects.
901 *Bulletin of the Seismological Society of America*, *92*(1), 376–386.
- 902 Papaleo, E., Cornwell, D., & Rawlinson, N. (2018). Constraints on North Anato-
903 lian Fault Zone width in the crust and upper mantle from S wave teleseismic
904 tomography. *Journal of Geophysical Research: Solid Earth*, *123*(4), 2908–2922.
- 905 Parsons, T., Toda, S., Stein, R. S., Barka, A., & Dieterich, J. H. (2000). Heightened odds
906 of large earthquakes near istanbul: An interaction-based probability calculation.
907 *Science*, *288*(5466), 661–665.
- 908 Perfettini, H., & Avouac, J.-P. (2004). Postseismic relaxation driven by brittle creep:
909 A possible mechanism to reconcile geodetic measurements and the decay
910 rate of aftershocks, application to the chi-chi earthquake, taiwan. *Journal of*
911 *Geophysical Research: Solid Earth*, *109*(B2).
- 912 Pınar, A., Üçer, S., Honkura, Y., Sezgin, N., Ito, A., Barış, Ş., ... Horiuchi, S. (2010). Spa-
913 tial variation of the stress field along the fault rupture zone of the 1999 Izmit
914 earthquake. *Earth, planets and space*, *62*(3), 237–256.
- 915 Poupinet, G., Ellsworth, W., & Frechet, J. (1984). Monitoring velocity variations
916 in the crust using earthquake doublets: An application to the calaveras fault,
917 california. *Journal of Geophysical Research: Solid Earth*, *89*(B7), 5719–5731.
- 918 Poyraz, S. A., Teoman, M. U., Türkelli, N., Kahraman, M., Cambaz, D., Mutlu, A., ... oth-
919 ers (2015). New constraints on micro-seismicity and stress state in the western
920 part of the North Anatolian Fault Zone: Observations from a dense seismic
921 array. *Tectonophysics*, *656*, 190–201.
- 922 Raub, C., Martínez-Garzón, P., Kwiątek, G., Bohnhoff, M., & Dresen, G. (2017). Varia-
923 tions of seismic b-value at different stages of the seismic cycle along the north
924 anatolian fault zone in northwestern turkey. *Tectonophysics*, *712*, 232–248.

- 925 Reilinger, R., Ergintav, S., Bürgmann, R., McClusky, S., Lenk, O., Barka, A., ... others
 926 (2000). Coseismic and postseismic fault slip for the 17 august 1999, $m=7.5$,
 927 izmit, turkey earthquake. *Science*, 289(5484), 1519–1524.
- 928 Reilinger, R., McClusky, S., Vernant, P., Lawrence, S., Ergintav, S., Cakmak, R., ... others
 929 (2006). GPS constraints on continental deformation in the Africa-Arabia-
 930 Eurasia continental collision zone and implications for the dynamics of plate
 931 interactions. *Journal of Geophysical Research: Solid Earth*, 111(B5).
- 932 Ross, Z. E., Trugman, D. T., Hauksson, E., & Shearer, P. M. (2019). Searching for hid-
 933 den earthquakes in Southern California. *Science*, eaaw6888.
- 934 Scholz, C. (1968). Microfractures, aftershocks, and seismicity. *Bulletin of the Seismo-
 935 logical Society of America*, 58(3), 1117–1130.
- 936 Scholz, C. H. (1968). The frequency-magnitude relation of microfracturing in rock and
 937 its relation to earthquakes. *Bulletin of the seismological society of America*, 58(1),
 938 399–415.
- 939 Scholz, C. H. (1998). Earthquakes and friction laws. *Nature*, 391(6662), 37–42.
- 940 Scholz, C. H. (2015). On the stress dependence of the earthquake b value. *Geophys-
 941 ical Research Letters*, 42(5), 1399–1402.
- 942 Shelly, D. R., Beroza, G. C., & Ide, S. (2007). Non-volcanic tremor and low-frequency
 943 earthquake swarms. *Nature*, 446(7133), 305.
- 944 Skarbak, R. M., Rempel, A. W., & Schmidt, D. A. (2012). Geologic heterogeneity can
 945 produce aseismic slip transients. *Geophysical Research Letters*, 39(21).
- 946 Smalley Jr, R. F., Chatelain, J.-L., Turcotte, D. L., & Prévot, R. (1987). A fractal ap-
 947 proach to the clustering of earthquakes: applications to the seismicity of the
 948 new hebrides. *Bulletin of the Seismological Society of America*, 77(4), 1368–
 949 1381.
- 950 Stein, R. S., Barka, A. A., & Dieterich, J. H. (1997). Progressive failure on the North
 951 Anatolian fault since 1939 by earthquake stress triggering. *Geophysical Journal
 952 International*, 128(3), 594–604.
- 953 Taylor, G., Rost, S., Houseman, G. A., & Hillers, G. (2019). Near-surface structure of
 954 the North Anatolian Fault zone from Rayleigh and Love wave tomography using
 955 ambient seismic noise. *Solid Earth*, 10(2), 363–378.
- 956 Toksoz, M., Reilinger, R., Doll, C., Barka, A., & Yalcin, N. (1999). Izmit (Turkey) earth-
 957 quake of 17 August 1999: first report. *Seismological Research Letters*, 70(6),
 958 669–679.
- 959 Toksöz, M., Shakal, A., & Michael, A. (1979). Space-time migration of earthquakes
 960 along the North Anatolian fault zone and seismic gaps. *Pure and Applied Geo-
 961 physics*, 117(6), 1258–1270.
- 962 Tormann, T., Wiemer, S., Metzger, S., Michael, A., & Hardebeck, J. L. (2013). Size
 963 distribution of parkfield's microearthquakes reflects changes in surface creep
 964 rate. *Geophysical Journal International*, 193(3), 1474–1478.
- 965 Trugman, D. T., & Shearer, P. M. (2017). GrowClust: A hierarchical clustering algo-
 966 rithm for relative earthquake relocation, with application to the Spanish Springs
 967 and Sheldon, Nevada, earthquake sequences. *Seismological Research Letters*,
 968 88(2A), 379–391.
- 969 Utkucu, M., Nalbant, S. S., McCloskey, J., Steacy, S., & Alptekin, Ö. (2003). Slip dis-
 970 tribution and stress changes associated with the 1999 november 12, düzce
 971 (turkey) earthquake ($m_w=7.1$). *Geophysical Journal International*, 153(1), 229–
 972 241.
- 973 Utsu, T. (1966). A statistical significance test of the difference in b -value between
 974 two earthquake groups. *Journal of Physics of the Earth*, 14(2), 37–40.
- 975 Waldhauser, F., & Ellsworth, W. L. (2000). A double-difference earthquake location
 976 algorithm: Method and application to the northern hayward fault, california.
 977 *Bulletin of the Seismological Society of America*, 90(6), 1353–1368.
- 978 White, M. C., Fang, H., Nakata, N., & Ben-Zion, Y. (2020). PyKonal: A Python Package
 979 for Solving the Eikonal Equation in Spherical and Cartesian Coordinates Using

- 980 the Fast Marching Method. *Seismological Research Letters*, 91(4), 2378–2389.
- 981 Wiemer, S., & Katsumata, K. (1999). Spatial variability of seismicity parameters in
982 aftershock zones. *Journal of Geophysical Research: Solid Earth*, 104(B6), 13135–
983 13151.
- 984 Wiemer, S., & Wyss, M. (1997). Mapping the frequency-magnitude distribution in as-
985 perities: An improved technique to calculate recurrence times? *Journal of Geo-
986 physical Research: Solid Earth*, 102(B7), 15115–15128.
- 987 Zhu, W., & Beroza, G. C. (2019). PhaseNet: a deep-neural-network-based seismic
988 arrival-time picking method. *Geophysical Journal International*, 216(1), 261–273.